An overview of recent physics results from NSTX

S.M. Kaye[1], **T. Abrams**[1], **J.-W. Ahn**[2], **J.P. Allain**[3], **R. Andre**[1], **D. Andruczyk**[3], **R. Barchfeld**[4], **D. Battaglia**[1], **A. Bhattacharjee**[1], **F. Bedoya**[3], **R.E. Bell**[1], **E. Belova**[1], **J. Berkery**[5], **L. Berry**[2], **N. Bertelli**[1], **P. Beiersdorfer**[6], **J. Bialek**[5], **R. Bilato**[7], **J. Boedo**[8], **P. Bonoli**[9], **A. Boozer**[5], **A. Bortolon**[10], **M.D. Boyer**[1], **D. Boyle**[1], **D. Brennan**[11], **J. Breslau**[1], **J. Brooks**[12], **R. Buttery**[13], **A. Capece**[1], **J. Canik**[2], **C.S. Chang**[1], **N. Crocker**[14], **D. Darrow**[1], **W. Davis**[1], **L. Delgado-Aparicio**[1], **A. Diallo**[1], **D. D'Ippolito**[15], **C. Domier**[4], **F. Ebrahimi**[11], **S. Ethier**[1], **T. Evans**[13], **N. Ferraro**[13], **J. Ferron**[13], **M. Finkenthal**[16], **R. Fonck**[17], **E. Fredrickson**[1], **G.Y. Fu**[1], **D. Gates**[1], **S. Gerhardt**[1], **A. Glasser**[18], **N. Gorelenkov**[1], **M. Gorelenkova**[1], **I. Goumiri**[11], **T. Gray**[2], **D. Green**[2], **W. Guttenfelder**[1], **R. Harvey**[19], **A. Hassanein**[12], **W. Heidbrink**[20], **Y. Hirooka**[21], **E.B. Hooper**[6], **J. Hosea**[1], **D. Humphreys**[13], **E.F. Jaeger**[22], **T. Jarboe**[18], **S. Jardin**[1], **M.A. Jaworski**[1], **R. Kaita**[1], **C. Kessel**[1], **K. Kim**[1], **B. Koel**[11], **E. Kolemen**[1], **G. Kramer**[1], **S. Ku**[1], **S. Kubota**[14], **R.J. LaHaye**[13], **L. Lao**[13], **B.P. LeBlanc**[1], **F. Levinton**[23], **D. Liu**[20], **J. Lore**[11], **M. Lucia**[3], **N. Luhmann Jr**[14], **R. Maingi**[1], **R. Majeski**[1], **D. Mansfield**[1], **R. Maqueda**[23], **G. McKee**[17], **S. Medley**[1], **E. Meier**[6], **J. Menard**[1], **D. Mueller**[1], **T. Munsat**[24], **C. Muscatello**[4], **J. Myra**[15], **B. Nelson**[18], **J. Nichols**[1], **M. Ono**[1], **T. Osborne**[13], **J.-K. Park**[1], **W. Peebles**[14], **R. Perkins**[1], **C. Phillips**[1], **M. Podesta**[1], **F. Poli**[1], **R. Raman**[18], **Y. Ren**[1], **J. Roszell**[11], **C. Rowley**[11], **D. Russell**[15], **D. Ruzic**[3], **P. Ryan**[2], **S.A. Sabbagh**[5], **E. Schuster**[25], **F. Scotti**[6], **Y. Sechrest**[24], **K. Shaing**[17], **T. Sizyuk**[12], **V. Sizyuk**[3], **C. Skinner**[1], **D. Smith**[17], **P. Snyder**[13], **W. Solomon**[1], **C. Sovenic**[17], **V. Soukhanovskii**[6], **E. Startsev**[1], **D. Stotler**[1], **B. Stratton**[1], **D. Stutman**[16], **C. Taylor**[12], **G. Taylor**[1], **K. Tritz**[16], **M. Walker**[13], **W. Wang**[1], **Z. Wang**[1], **R. White**[1], **J.R. Wilson**[1], **B. Wirth**[10], **J. Wright**[9], **X. Yuan**[1], **H. Yuh**[23], **L. Zakharov**[1] and **S.J. Zweben**[1]

[1] Princeton Plasma Physics Laboratory, Princeton University, Princeton, NJ 08543, USA
[2] Oak Ridge National Laboratory, Oak Ridge, TN 37831, USA
[3] University of Illinois at Urbana-Champaign, Urbana, IL, USA
[4] University of California at Davis, Davis, CA, USA
[5] Columbia University, New York, NY, USA
[6] Lawrence Livermore National Laboratory, Livermore, CA, USA
[7] IPP, Garching, Germany
[8] University of California at San Diego, San Diego, CA, USA
[9] Massachusetts Institute of Technology, Cambridge, MA, USA
[10] University of Tennessee, Knoxville, TN, USA
[11] Princeton University, Princeton, NJ, USA
[12] Purdue University, W. Lafayette, IN, USA
[13] General Atomics, San Diego, CA, USA
[14] University of California at Los Angeles, Los Angeles, CA, USA
[15] Lodestar Research Corporation, Boulder, CO, USA
[16] Johns Hopkins University, Baltimore, MD, USA
[17] University of Wisconsin, Madison, WI, USA
[18] University of Washington, Seattle, WA, USA
[19] CompX, Del Mar, CA, USA
[20] University of California at Irvine, Irvine, CA, USA
[21] National Institute for Fusion Science, Oroshi, Toki, Gifu, Japan
[22] XCEL, Oak Ridge, TN, USA
[23] Nova Photonics, Princeton, NJ, USA
[24] University of Colorado, Boulder, CO, USA
[25] Lehigh University, Bethlehem, PA, USA

E-mail: skaye@pppl.gov

CrossMark

Abstract

The National Spherical Torus Experiment (NSTX) is currently being upgraded to operate at twice the toroidal field and plasma current (up to 1 T and 2 MA), with a second, more tangentially aimed neutral beam (NB) for current and rotation control, allowing for pulse lengths up to 5 s. Recent NSTX physics analyses have addressed topics that will allow NSTX-Upgrade to achieve the research goals critical to a Fusion Nuclear Science Facility. These include producing stable, 100% non-inductive operation in high-performance plasmas, assessing plasma–material interface (PMI) solutions to handle the high heat loads expected in the next-step devices and exploring the unique spherical torus (ST) parameter regimes to advance predictive capability. Non-inductive operation and current profile control in NSTX-U will be facilitated by co-axial helicity injection (CHI) as well as radio frequency (RF) and NB heating. CHI studies using NIMROD indicate that the reconnection process is consistent with the 2D Sweet–Parker theory. Full-wave AORSA simulations show that RF power losses in the scrape-off layer (SOL) increase significantly for both NSTX and NSTX-U when the launched waves propagate in the SOL. Toroidal Alfvén eigenmode avalanches and higher frequency Alfvén eigenmodes can affect NB-driven current through energy loss and redistribution of fast ions. The inclusion of rotation and kinetic resonances, which depend on collisionality, is necessary for predicting experimental stability thresholds of fast growing ideal wall and resistive wall modes. Neutral beams and neoclassical toroidal viscosity generated from applied 3D fields can be used as actuators to produce rotation profiles optimized for global stability. DEGAS-2 has been used to study the dependence of gas penetration on SOL temperatures and densities for the MGI system being implemented on the Upgrade for disruption mitigation. PMI studies have focused on the effect of ELMs and 3D fields on plasma detachment and heat flux handling. Simulations indicate that snowflake and impurity seeded radiative divertors are candidates for heat flux mitigation in NSTX-U. Studies of lithium evaporation on graphite surfaces indicate that lithium increases oxygen surface concentrations on graphite, and deuterium–oxygen affinity, which increases deuterium pumping and reduces recycling. *In situ* and test-stand experiments of lithiated graphite and molybdenum indicate temperature-enhanced sputtering, although that test-stand studies also show the potential for heat flux reduction through lithium vapour shielding. Non-linear gyro kinetic simulations have indicated that ion transport can be enhanced by a shear-flow instability, and that non-local effects are necessary to explain the observed rapid changes in plasma turbulence. Predictive simulations have shown agreement between a microtearing-based reduced transport model and the measured electron temperatures in a microtearing unstable regime. Two Alfvén eigenmode-driven fast ion transport models have been developed and successfully benchmarked against NSTX data. Upgrade construction is moving on schedule with initial physics research operation of NSTX-U planned for mid-2015.

Keywords: NSTX, spherical torus, overview

(Some figures may appear in colour only in the online journal)

1. Introduction

Recent analysis of data from the National Spherical Torus Experiment (NSTX) has focused on topics critical to the development of the research plan and achievement of physics goals for the NSTX-Upgrade. NSTX ($R/a = 0.85/0.65$ m, $\kappa = 1.8$–2.4, $\delta = 0.3$–0.8, I_p up to 1.5 MA, B_T up to 0.55 T) concluded operation in October 2010 in order to begin Upgrade construction activities. NSTX-U [1] has three primary research goals:

1. To advance the spherical torus (ST) concept for a fusion nuclear science facility (FNSF) [2]. Achieving this goal requires demonstrating 100% non-inductive sustainment at a performance level that extrapolates to $\geqslant 1$ MW m^{-2} neutron wall loading in FNSF, as well as developing non-inductive start-up and ramp-up techniques for an FNSF with a small, or no, solenoid. The latter is a particularly unique requirement for an ST-based FNSF [3].

2. To develop solutions for the plasma–material interface (PMI). High-flux expansion snowflake or X-divertor, coupled with radiative detachment, will be employed for mitigating high heat fluxes ($q_{peak,div} \simeq 40$ MW m^{-2},

$P_{heat}/S \simeq 0.5$ MW m^{-2}, up to five times greater than in NSTX), and high-Z and liquid lithium plasma-facing components (PFC) will be assessed as PMI solutions.

3. To explore unique ST parameter regimes to advance predictive capability for ITER and beyond. In order to address this goal, NSTX-U will access reduced collisionality (up to a factor of ten lower than that in NSTX) and high-β ($\beta_n \leqslant 6$) with an ability to vary the q- and rotation profiles for enhanced stability, confinement and non-inductive current drive. Models for thermal and fast ion transport will be developed and/or tested.

The increased capabilities of NSTX-U ($R/a = 0.95/0.55$ m, $\kappa \simeq 2.8$) will facilitate the research necessary to achieve these goals. The major capabilities include a factor of $\sim$two increase in both plasma current I_p and toroidal magnetic field B_T to 2 MA and 1 T respectively, and an additional off-axis neutral beam that will double the available nominal input beam power to 12 MW. The first two enhancements will allow for high-β operation at almost an order-of-magnitude lower collisionality [4], and the second neutral beam, coupled with up to 6 MW of high harmonic fast wave (HHFW) heating and current drive, will provide means to vary the q- and rotation

profile, and it will provide significant non-inductive current drive directly or indirectly. This will enable NSTX-U to sustain stable, high-performance discharges in near steady-state conditions for pulse lengths up to 5 s, which is a duration of many current diffusion times. Advanced control algorithms, using the above capabilities as well as applied $n = 1$ to 3 non-axisymmetric magnetic perturbations (MPs) from a midplane, and eventually, possibly an off-midplane, coil system will be utilized for stable operation. A cryo-pump is being considered for density control. A disruption prediction, avoidance and mitigation (PAM) system will be deployed using a large number of measurements and models for prediction and avoidance [5–7] and a massive gas injection (MGI) system at different poloidal locations to optimize gas penetration for reducing potential wall damage due to disruptive forces. Lithium evaporation and boronization will be used as the primary wall conditioning techniques, and off-line research centred on liquid lithium on metal substrates will support a planned phasing in of high-Z PFCs.

The capabilities of NSTX-U complement those of the companion ST, MAST-U [8], which plans to commence operation shortly after the start of NSTX-U. The elements of recent research on NSTX-U, both experimental analysis and theory that address the topics mentioned above, will be reported in this paper.

2. Advance the ST concept for a Fusion Nuclear Science Facility

This section will focus on two main issues, the non-inductive current drive research that will allow for achievement of the 100% non-inductive goal in the three phases of the discharge (start-up, ramp-up and sustainment), and the ability to maintain magnetohydrodynamic (MHD) stable plasmas for long duration.

2.1. Non-inductive start-up and ramp-up

NSTX-U is striving for fully non-inductive operation to establish the physics basis of an ST-FNSF with small or no solenoid, and the starting point is plasma initiation and current ramp-up. An envisioned strategy for non-inductive operation in NSTX-U is shown in figure 1. NSTX-U will initiate the plasma using co-axial helicity injection (CHI), as has been done in NSTX [9]. Plasma guns [10] will be tested on NSTX-U for start-up once development on smaller devices is complete. Once the plasma is initiated, electron cyclotron heating (ECH) is being considered for heating the plasma from an initial temperature of 10 s of eV to up to several hundred eV, along with HHFW to heat the plasma further to the 1–3 keV level (red phase). At this point, HHFW and/or neutral beam injection (NBI) current drive would be used to ramp the plasma current up to full current (blue phase), at which time neutral beam current drive and bootstrap current would be utilized to sustain the full current non-inductively (black phase).

CHI has been successfully used for plasma formation in NSTX with currents up to 200 kA and especially with coupling to inductive ramp-up [9]. Axisymmetric Tokamak Simulation Code (TSC) [11] simulations, reported previously [12], have been validated successfully against NSTX discharges,
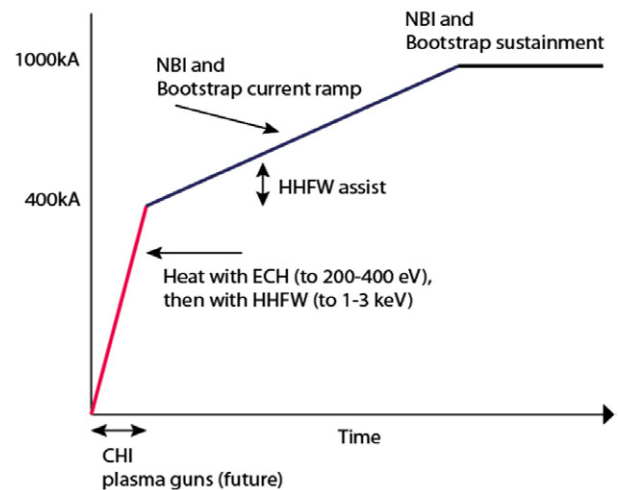

Figure 1. Strategy for fully non-inductive operation in NSTX-U.

and these simulations are the basis for start-up scenario development on NSTX-U, where CHI is projected to be able to provide up to 400 kA of start-up current. An example of the TSC-produced flux evolution in an NSTX plasma is shown in figure 2. For this case, a 5 ms voltage pulse is applied across the injection electrodes, providing sufficient current to allow the discharge to fill the vessel. The voltage is rapidly reduced to zero at $t = 5$ ms (first panel in figure 2). The closed flux surfaces form in this axisymmetric simulation as a result of generation of a strong toroidal loop voltage that drives the toroidal current.

The underlying physics of CHI start-up have been studied with resistive MHD simulations using the NIMROD code [13] in 2D in order to improve the flux surface closure and current drive using this technique [14, 15]. In one set of simulations, time-varying boundary conditions and poloidal field coil currents emulating experimental conditions were used, and closed flux surfaces were produced [14]. A more simplified model, with constant poloidal field currents and time varying injector currents, was used to study the minimum conditions for flux closure [15]. In these simulations, the injector voltage is adjusted so that the $J \times B$ force overcomes the field line tension and open field lines fill the vessel. Flux closure occurs under the right conditions approximately 0.5 ms after the injector voltage is turned off, as in the experiment.

These simulations indicate that the magnetic diffusivity strongly controls flux closure, with no flux closure at high diffusivity corresponding to temperatures lower ($T_e \simeq 1$ eV) than those measured in the experiment. As the diffusivity decreases with T_e increasing towards the experimental values (10–25 eV), flux closure occurs with increasing volume of closed flux. Field line tracing was used to confirm the formation of the X-point and flux closure, as is shown in figure 3 for two temperatures, $T_e = 14$ and 24 eV. Additional scans indicate other dependences controlling flux closure. If the injection voltage is slowly reduced to zero or the injector flux footprints are too far apart, closure is inhibited. The first is due to smaller generated toroidal loop voltage, and the second due to the longer time scales required for the oppositely directed flux to come together and form an X-point.
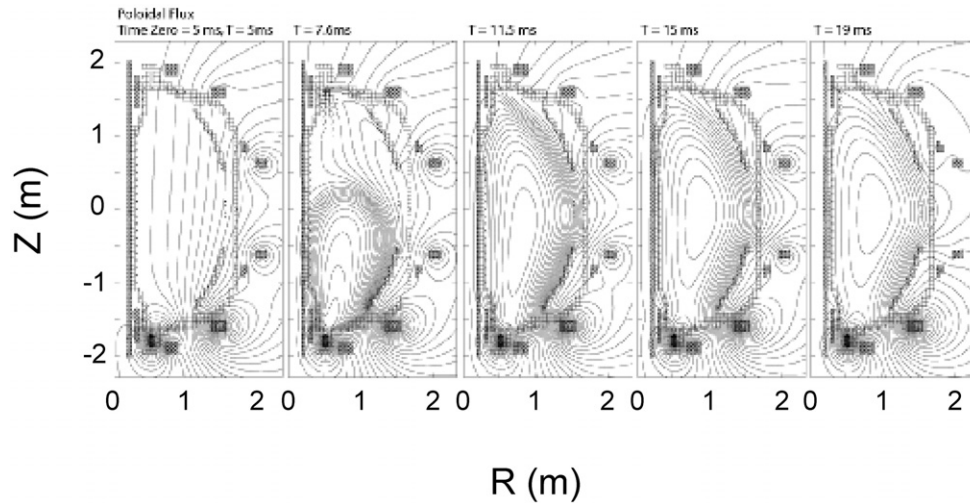
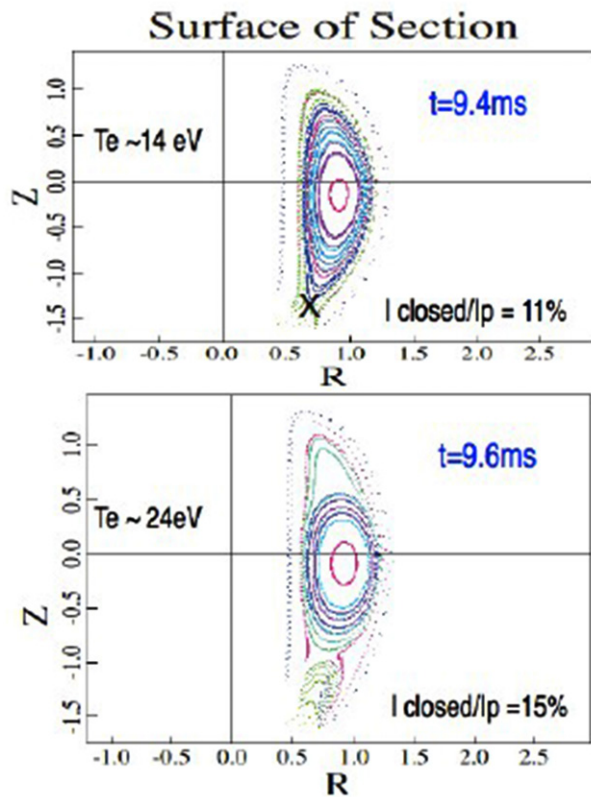**Figure 2.** Time evolution of flux surface closure with CHI in an NSTX plasma.

Figure 3. Poincaré plots soon after flux closure for two experimentally relevant electron temperatures (*a*) 14 eV and (*b*) 24 eV [15]. (Copyright 2013, American Institute of Physics.)
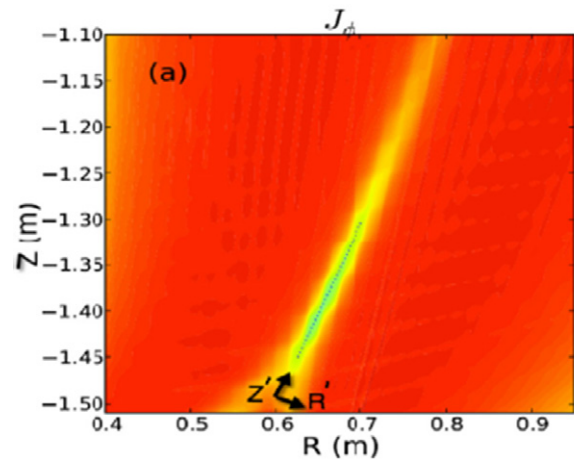

Figure 4. Toroidal current in the reconnection region. [14, 15]. (Copyright 2013, American Institute of Physics.)

The simulations have shown that during X-point formation, the current density is localized to an elongated current sheet (figure 4) whose width scales as $\eta^{1/2}$, where η is the magnetic diffusivity. This, along with the computed strong inflow and outflow characteristics, suggests that the X-point formation may be a Sweet–Parker-type reconnection.

Once the plasma is initiated, the core electron temperature has to be increased in order for HHFW or NBI to couple to the NSTX-U plasma for continued ramp-up of the plasma current.

In order to do this, and as part of a possible future upgrade to the NSTX-U facility, a 28 GHz O-mode ECH system that is capable of injecting $\geqslant 1$ MW for pulse lengths of up to several seconds can be utilized. TSC simulations predict that the central electron temperature can increase from 10 to 100 eV in 20 ms when 0.6 MW of ECH power is coupled to a CHI plasma. This increase in temperature will reduce significantly the plasma current decay rate of CHI plasmas and allow for coupling to medium and high harmonic fast wave heating and NBI.

The level of heating and current drive that HHFW can provide is critically dependent on how much power is lost along open field lines in the SOL. Recent experimental results have shown that up to 60% of the coupled power can be lost when edge densities are high enough that fast waves can propagate close to the launcher [16]. Thus, it is important to understand the physics of RF deposition and especially this edge loss mechanism in order to optimize discharge scenarios that lead to RF loss minimization. Understanding the physics can aid in the projection to ICRF efficiency and deposition in ITER.
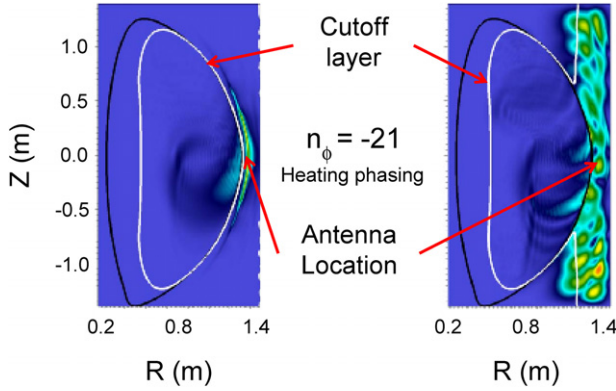
Figure 5. Wave electric field from AORSA for low density, $n_{SOL} = 1 \times 10^{18}\,\mathrm{m^{-3}}$, (left) and high density, $n_{SOL} = 2 \times 10^{18}\,\mathrm{m^{-3}}$, (right) at the front of the antenna. (Adapted from [18] courtesy of IAEA.)

Full-wave simulations using the AORSA code [17] have been performed to demonstrate the direct correlation between the location of the fast wave cutoff relative to the antenna and the last closed flux surface (LCFS), the large amplitude of the RF fields in the SOL, and the power loss there [18]. Figure 5 shows the wave electric field obtained from AORSA for an NSTX discharge in which, for the computation, two density values in front of the antenna were used. The white and black curves in the figure indicate the FW cutoff and LCFS, respectively. It is clearly seen in the figure that the wave electric field in the SOL is small at a low density, when the FW cutoff is in front of the antenna, but becomes quite large at a high density when the FW cutoff opens up. At a low density, when the cutoff is in front of the antenna, the waves are evanescent, but they can propagate in the scrape-off layer (SOL) when the cutoff opens at a high density.

In order to understand how the variation of the electric field amplitude is associated with the wave SOL power losses, an artificial collisional damping has been incorporated into AORSA. The actual damping mechanism is presently unknown. The fraction of RF power lost to the SOL as a function of density in front of the antenna, n_{ant}, for two different toroidal wave numbers is shown in figure 6. In the figure, the vertical lines reflect the density at which the FW cutoff opens up for the respective wavenumbers. The figure shows the rapid increase of lost power as the wave transitions from the evanescent (low n_{ant}) to the propagating (high n_{ant}) regime, where the wave electric field amplitude is calculated to be low and high, respectively. The value of the collisional damping term has been chosen so that the level of RF power loss to the SOL is consistent with levels inferred from experiment for the conditions studied [18].

These calculations have been extended to NSTX-U, and the results indicate the same transition behaviour as a function of n_{ant} as was found for NSTX. An important difference, however, is that the transition to high losses is predicted to occur at higher densities ($2\times$) in NSTX-U, indicating a wider SOL density range in which the experiment can run with lower SOL power losses. This is because $n_{SOL,cutoff} \propto k_{\parallel}^2 B_T/\omega$. Future studies will also work on identifying the actual physical mechanism(s) behind the RF power losses.
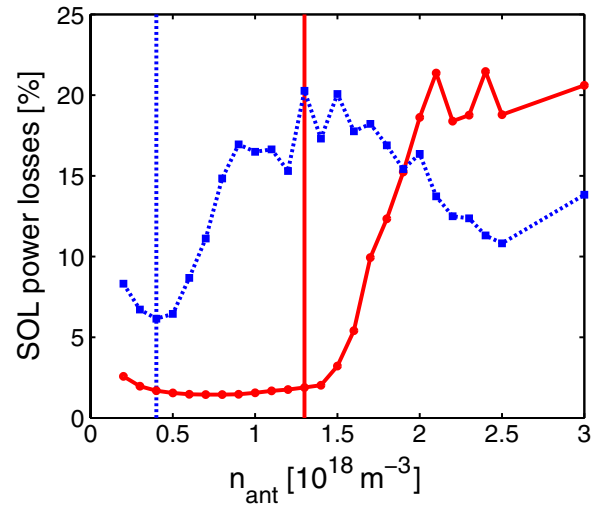

Figure 6. Fraction of power lost to the SOL as a function of density in front of the antenna for $n_{\phi} = -21$ (solid red) and $n_{\phi} = -12$ (dashed blue) as calculated by AORSA. The vertical lines indicate the cutoff density for the two respective n_{ϕ}. (Reproduced from [18] courtesy of IAEA.)
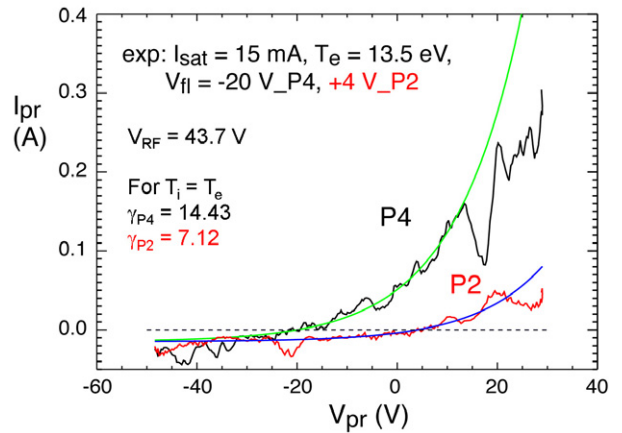

Figure 7. $I-V$ characteristic for probes P4 ($R = 70.59\,\mathrm{cm}$, under spiral) and P2 ($R = 64.67\,\mathrm{m}$, away from spiral).

Field-aligned RF losses in the SOL have been shown to produce bright hot spirals in the NSTX lower outer divertor [19]. An analysis of the $I-V$ characteristics of a radial array of swept Langmuir probes [20] in the lower divertor indicates that RF rectification may be an important contributor to the heat flux to the probe under the spiral [21]. The RF fields produce a negative shift in the floating potential of $-24\,V$ for the probe under the spiral (P4 at $R = 70.59\,\mathrm{m}$) relative to that away from the tile (P2 at $R = 64.67\,\mathrm{m}$), as is seen in figure 7. Both probe characteristics, however, have similar I_{sat} and T_e values, indicating that the sheath heat flux transmission factor, $\gamma = q_{heat}/j_{sat}T_e$, doubles for the rectified ($-24\,V$ offset) case. The importance of this is that the tile heating may be a result of a process (rectification) close to the tiles, rather than a process that takes place along the field line. The latter could potentially result in a difference in temperature between the P2 and P4 probes, which is not seen (figure 7). Furthermore, the source of the floating potential offset may be related to the large wave electric fields seen in figure 5, as this rectification
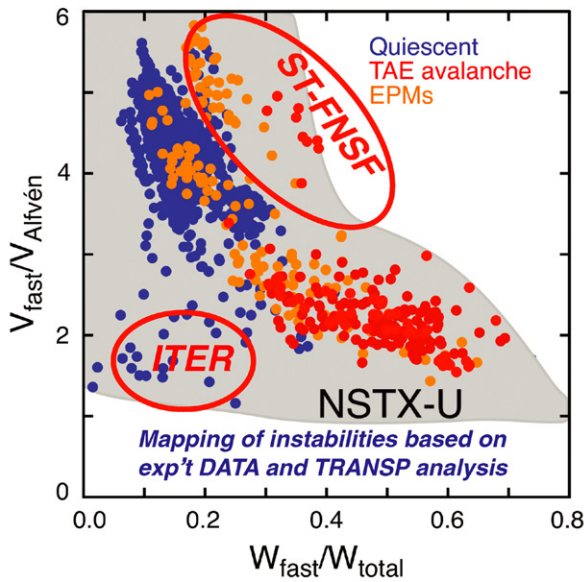
Figure 8. Existence space for various types of Alfvén activity in NSTX.

Figure 9. (Top) Spectrogram of envelope of high-frequency CAE fluctuation amplitude, overlaid with kink mode frequencies. (Bottom) Relative phase between the $n = 1$ kink and high-frequency CAE envelope [23]. (Copyright 2013, American Institute of Physics.)

appears to be stronger when the spirals are stronger, which is at a higher n_{ant} [21]. Rectification as a source for tile heating, which may be an issue for ITER, will be studied further on NSTX-U with a more comprehensive set of Langmuir probes, both in location and diagnostic capability.

2.2. Non-inductive sustainment: energetic particle physics and neutral beam current drive

Neutral beam current drive will be used during both the discharge ramp-up and sustainment phases to aid the achievement of 100% non-inductive operation. NSTX-U will have two neutral beam injectors, each with three sources, aiming at $R = 0.5, 0.6, 0.7$ m and $1.1, 1.2, 1.3$ m for a nominal plasma major radius of 0.95 m. The beams will provide the capability not only to drive current, but also to tailor the current profiles for stable operation [4]. It is, however, important to understand the physics processes that can affect the fast ion distribution in order to develop scenarios to achieve the NSTX-U research goals and to address the performance of future fusion plasma experiments such as ITER. Figure 8 is an existence plot of the types of Alfvén activity seen in NSTX as a function of $v_{fast}/v_{Alfvén}$ and W_{fast}/W_{total}. Generally, NSTX discharges evolve from the lower right of the figure to the upper left as the density increases. Toroidal Alfvén eigenmode (TAE) avalanches and other energetic particle modes (EPMs) are observed at higher W_{fast}/W_{total} (low and medium density), while EPMs and quiescent plasmas are seen at lower W_{fast}/W_{total} (higher densities). TAE avalanches are seen when $W_{fast}/W_{total} \geqslant 0.3$. The figure also shows that the NSTX-U operational space (grey shaded region) in these parameters overlaps that envisioned for both ITER and an ST-FNSF. The TAE avalanches and EPMs can result in up to a 35% drop in the neutron rate, which has been determined to come primarily from energy loss and spatial redistribution of the fast ions [22]. This conclusion is based on the determination of the linear eigenmode structure whose mode amplitudes are constrained by measured displacements, and particle tracking
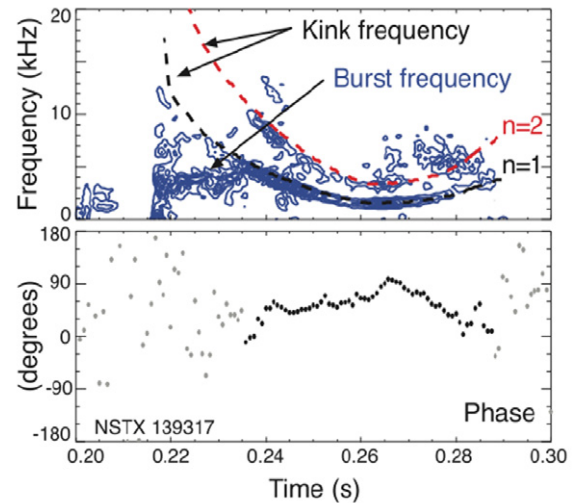
in the presence of these modes. Further, the analysis of individual TAE avalanches indicates that the energy lost from the fast ions is comparable to the estimated wave energy lost due to TAE damping on the thermal plasma.

Recent analysis and theory have also revealed complex relationships between different instabilities. Figure 9 shows an example of high-frequency (1.4–2 MHz) compressional Alfvén eigenmode (CAE) whose burst frequency is regulated by kink modes in the 2–30 kHz frequency range [23]. The CAE burst frequency clearly locks on the $n = 1$ and 2 kink mode frequencies (top panel), with a phase shift of $\sim 90°$ (bottom panel). This repetitive bursting of modes, and coupling to kinks with this phase shift, may indicate a predator–prey relation, where the fast ion beta takes the role of the prey, increasing linearly in the absence of mode-induced losses, and the CAE mode amplitude plays the role of the predator, causing fast ion loss. Simulations with a predator–prey model find that that just a few per cent modulation of the CAE damping rate is sufficient to cause the phase locking as is seen in the experiment [23].

In ST plasmas with weakly reversed magnetic shear and q_{min} slightly above 1, stability calculations [24] indicate that a non-resonant kink (NRK) can be unstable. NSTX discharges have exhibited the co-existence of the NRK with higher frequency, beam-driven fishbone modes (EPMs), and linear and non-linear simulations using the global kinetic/MHD hybrid M3D-K code [25] were carried out to study the energetic particle interaction with the NRK [26]. Figure 10 shows the map of mode stability as a function of q_{min} and $\beta_{hot}/\beta_{total}$ at a fixed input power. At lower q_{min}, the energetic ions are strongly stabilizing for the NRK (higher $\beta_{hot}/\beta_{total}$). At low fast ion population and low q_{min} (lower left of the figure), the mode structure (inset) reflects that of a pure MHD mode with zero mode frequency and up–down symmetric structure at zero toroidal angle. At higher fast particle population and higher q_{min}, the mode transitions to a fishbone-like EPM with a frequency comparable to the precession drift frequency. The mode structure (inset) has a twisted character. Both the
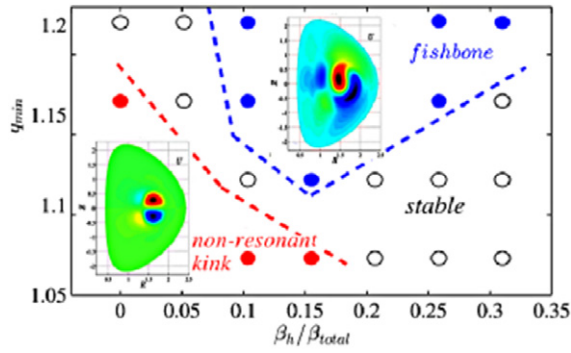
Figure 10. Mode stability for the NRK and fishbone modes in NSTX. Insets show the linear eigenmode structure [26]. (Copyright 2013, American Institute of Physics.)
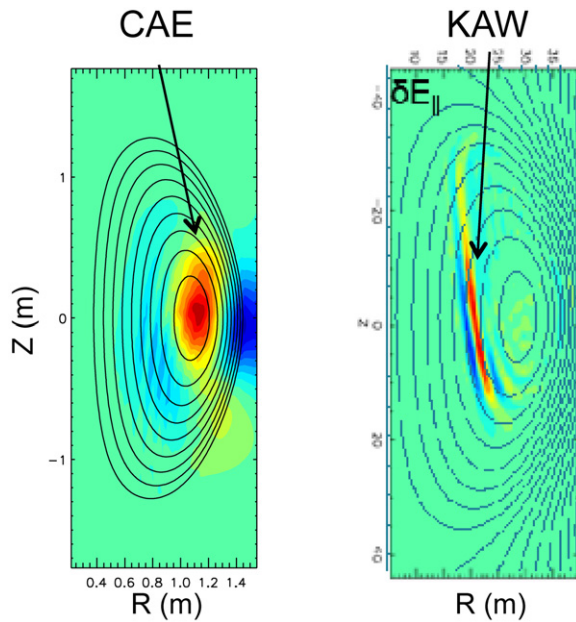

Figure 11. Contour plots of the parallel magnetic field perturbation for CAE (left) and perturbed electric field contours for KAW (right).

Figure 12. $\partial F_{\text{fast}}/\partial v_\perp$ at the parallel resonant velocity as computed by TRANSP and SPIRAL with (red) and without (black) applied MPs.

of energy flux away from the magnetic axis to the KAW resonance location; i.e. energy flows from the core CAE modes to the mid-radius KAW. Using the HYM-calculated linear mode structure, and by estimating the MP level from the reflectometer displacement measurements [29], up to 0.4 MW of power can be channelled out of the core, and this channelling could have a direct effect on the temperature profiles, with changes of calculated to be up to several hundred eV. This is one possible explanation for the lack of significant heating of the central T_e observed with increasing beam power and associated with CAE/GAE activity [30].

Alfvén eigenmodes (AEs) and fast ion populations can also be impacted significantly by the application of external 3D fields. Magnetic measurements of energetic ion-driven high-frequency bursting CAE/GAE modes have shown that applying a $\delta B/B \sim 0.1$ to 1% $n = 3$ MP at the plasma edge can lead to a reduction in mode amplitude, an increase in bursting frequency, and a smaller frequency chirp [31]. The change in mode characteristics is accompanied by a drop in neutron rate. This is due to a loss of fast ions due directly to the change in magnetic equilibrium by the application of the 3D field. The effect of this MP on the fast ion distribution was calculated using the SPIRAL [32] code to track the energetic particle distribution in the presence of 3D fields and a resistive plasma response calculated by the M3D-C^1 code [33]. Figure 12 shows the difference in $\partial F_{\text{fast}}/\partial v_\perp$ at the parallel resonant velocity with (red) and without (black) applied MPs, as calculated from the TRANSP [34] and SPIRAL codes. These simulations indicate a 10–20% reduction in $\partial F_{\text{fast}}/\partial v_\perp$, the main driving term for these high-frequency modes. The reduced drive is consistent with the experimentally observed reduction in mode amplitude when the 3D fields are applied.

It has also been observed that application of 3D MPs pulses can modulate TAE modes. As is seen in figure 13, 50–100 kHz modes are damped right after the application of the MP. 3D calculations were performed using the stellarator VMEC [35] and STELLOPT [36] codes to determine the 3D ideal MHD equilibrium and Alfvén continuum, respectively. It was found that in the presence of 3D MPs, AE gaps shrink, leading to an enhanced damping of the TAE by interaction with the continuum. These results indicate a possible path for

NRK and the fishbone modes significantly affect the fast ion distribution, reducing the fast ion density in the central region of the plasma. The results from these linear and non-linear M3D-K calculations will be used to identify the regimes for stable operation in NSTX-U.

The excitation of high-frequency global and compressional Alfvén modes has been studied for an NSTX H-mode discharge using the hybrid-MHD non-linear HYM code [27]. Co-rotating CAE modes were calculated to be unstable for a range of toroidal mode numbers, consistent with experimental observations [28]. Results from HYM indicated that unstable CAE modes can strongly couple to kinetic Alfvén waves (KAWs) on the high-field side of the torus, as is seen by the perturbed parallel magnetic field structure due to the CAE and by the perturbed parallel electric field for the KAW modes shown in figure 11. The resonance with the KAW is located at the edge of the CAE potential well, just inside the outer edge of the beam ion density profile. The importance of this result is that this coupling provides an energy channelling mechanism for beam energy to excite core CAE modes with a resulting transport
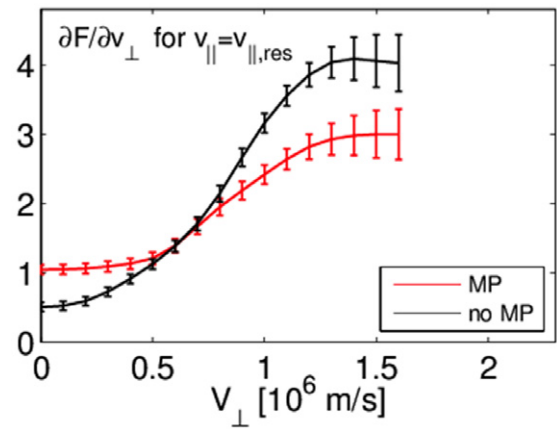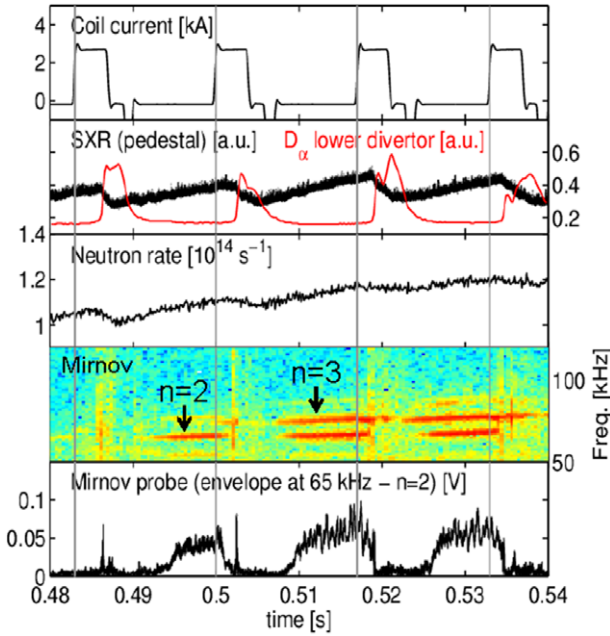
Figure 13. TAEs modulated by pulsed edge MPs.

Figure 14. Fully non-inductive current scenario for a 1 T NSTX-U discharge as computed by TRANSP with the ISOLVER free boundary equilibrium solver.

Figure 15. $n = 1$ RFA amplitude as a function of average plasma rotation frequency [7]. (Copyright 2014, American Institute of Physics.)

optimizing the MPs to produce a 3D perturbed equilibrium stable against AEs.

Time-dependent simulations with the free boundary equilibrium solver ISOLVER in TRANSP have begun in order to develop fully non-inductive 1 T NSTX-U discharge scenarios using current drive from all the systems discussed up to now. The simulation was run with the loop voltage constrained to be zero. TORAY [37, 38] simulations indicate that 1 MW of EC heating can rapidly heat plasmas generated by CHI. T_e increases from 10–20 eV, typical of CHI plasmas, to about 1 keV in 30 ms. Up to 4 MW of HHFW is then used in conjunction with EC to further heat the plasma and to drive current to facilitate NBI with minimal fast ion losses, as calculated by TORIC [39]. The combined EC/HHFW can delay the decrease of the CHI generated current and sustain a non-inductive current of 350 kA. With 10 MW of NBI distributed over the two beamlines, the simulation shows that the current can be ramped up non-inductively to 900 kA in 2.5 s. With the density between 60% and 90% of the Greenwald limit and $H_{98y,2} \simeq 1.0$ to 1.2, the total current is sustained with a contribution from the bootstrap between 40% and 60% for this simulation (figure 14). The simulation has not relaxed to a full steady state, and this results in a finite electric field inside the plasma which gives rise to the small, negative ohmic current.

2.3. Non-inductive sustainment: stable operations

The next step towards fully non-inductive operation is the ability to maintain MHD stability during the course of the current ramp-up and flattop phases. This will depend on the ability to control current, rotation and pressure profiles during these discharge phases, and simultaneously to provide sufficient non-inductive current drive. This subsection will focus on stability control methods. Recent work towards understanding the physics that will enable development of control algorithms will be discussed.
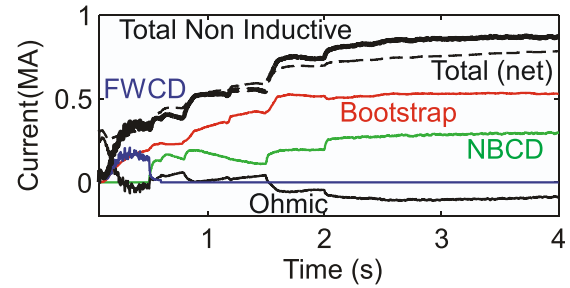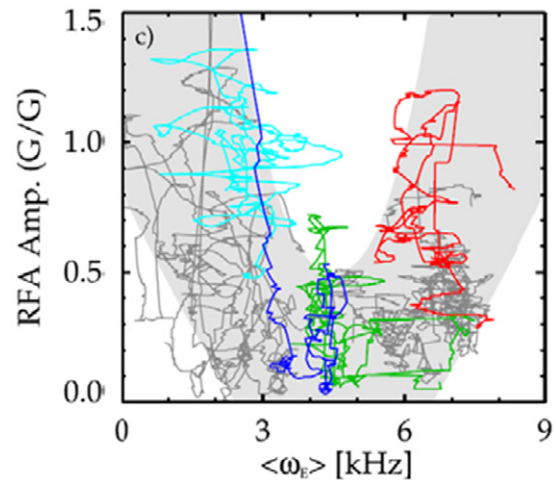
One requirement for stable operation is the ability to control the resistive wall mode (RWM) [40, 41]. Recent work on RWMs, including calculations with the MISK code [42, 43], has given a complex picture in which stability is controlled not only by collisional dissipation, but also by kinetic resonances and the plasma rotation profile [7, 44]. In particular, when the plasma rotation is resonant with one of the kinetic effects (e.g. precession drift or bounce motion), the RWM stability, as inferred from the resonant field amplification (RFA) measured by $n = 1$ MHD spectroscopy, shows a clear dependence on collisionality and β_n / l_i. Rotation is also critical, however, and this is shown in figure 15 where the RFA amplitude is plotted as a function of the average plasma $E \times B$ rotation frequency for an NSTX H-mode discharge [6, 7]. There is clearly an optimal value rotation profile for stable operation (minimum RFA amplitude), and at the corresponding value of $\langle \omega_E \rangle$ the plasma is on-resonance with the precession drift.

In order to control the plasma rotation, a coupled 1D toroidal rotation model and controller is being developed in order to capture and sustain a favourable plasma rotation profile. In this algorithm, the neoclassical toroidal viscosity (NTV) [45] and NB torque are used as actuators for the controller design. The rotation is governed by the simplified toroidal momentum equation, which balances the time rate of the change of rotation (assuming fixed density) with input torque and with a diffusive transport loss governed by an
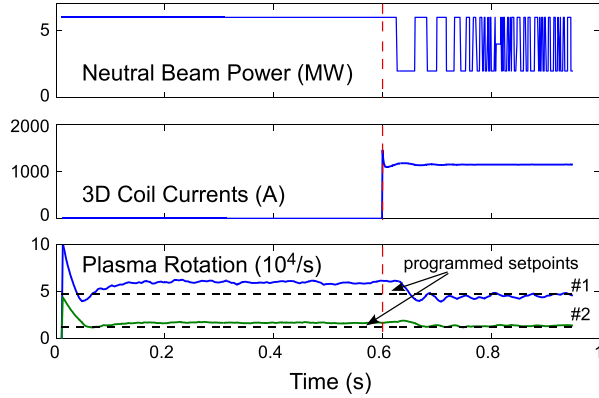
Figure 16. NTV and NBI actuators (top panels) and evolution of plasma rotation using rotation control algorithm. The two set points represent two different radii, $r/a = 0.13$ (set point #1) and $r/a = 0.55$ (set point #2).

Figure 17. Experimental NTV torque density (black) and that calculated from POCA (red).

Figure 18. Experimental NTV torque (green) and that calculated from NTVTOK scaled by a factor of 0.6.

effective momentum diffusivity. The NTV torque is given by a relation that is proportional to the product of the plasma rotation frequency and the square of the applied MP from the midplane coils. The NB torque is calculated in the NUBEAM [46] code in TRANSP. The two expressions are non-linear in the plasma rotation frequency, and they are solved and advanced in TRANSP. An example of the first use of this technique is shown in figure 16, which shows the NB and NTV torque (top panels) and plasma rotation evolution at two rotation set points ($r/a = 0.13$ and 0.55, respectively) from the rotation feedback control algorithm. In this example, the NTV was produced by $n = 3$ fields from the midplane MP coils. Using the combined NB and NTV torques, the rotation reaches its target in approximately 20 ms, much shorter than the momentum confinement time of ~ 150 ms [47], validating the use of this control algorithm in real time.

Understanding the underlying physics of NTV will allow for more confident use in predictions to future devices. Early experimental work showed quantitative agreement between the measured decrease in the toroidal angular momentum profile and the calculation of non-resonant drag torque based on NTV theory when the effect of toroidally trapped particles was included [48]. Several recent efforts have extended this work.

In one approach [49], the POCA (Particle Orbit Code for Anisotropic Pressure) code was developed to follow guiding centre orbits of particles for precisely calculating δf, the perturbed distribution function, in a non-axisymmetric ideal MHD equilibrium determined by IPEC [50]. POCA simulations show the importance of collisionality and particle resonances with the toroidal rotation, similar to that found for RWMs. A comparison of NTV torque density calculated by POCA with the measured dL/dt from changes in the momentum profile is shown in figure 17 for an $n = 3$ experiment. As can be seen, the NTV torque density magnitudes agree roughly in the $\Psi_n = 0.6$ to 0.8 region, although the location of the NTV peak is shifted inward in the POCA calculation, and POCA underestimates the NTV inside of $\Psi_n = 0.5$.

Another approach to determining the NTV computes the δB fully in 3D, and it uses the Shaing formulation of the NTV torque T_{NTV} valid for all collisionality regimes and the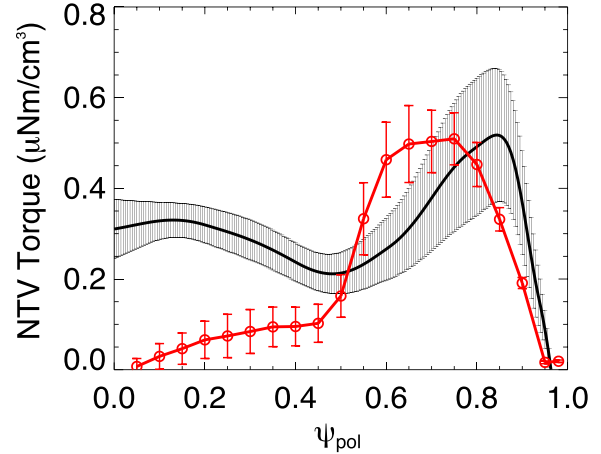 superbanana-plateau regime for both ions and electrons, as implemented in the NTVTOK code [51]. The calculation includes the effect of the flux surface displacement. Results from the code for an applied $n = 3$ configuration in NSTX are shown in figure 18. The calculated T_{NTV} exhibits large radial variations that are not observed experimentally. The calculated radial displacements are smaller than either the ion banana or gyroradii, suggesting finite orbit effects will spatially average T_{NTV}. The NTV torque density calculated from theory that is shown in figure 18 is, therefore, averaged over the banana width. The calculated NTV torque density is scaled by a factor of 0.6, and it closely matches the experimental dL/dt in the outer region of the plasma where the NTV is the strongest. In this outer region, the flux surface-averaged δB calculated by NTVTOK compares favourably with that computed by M3D-C^1, which includes a resistive plasma response model.
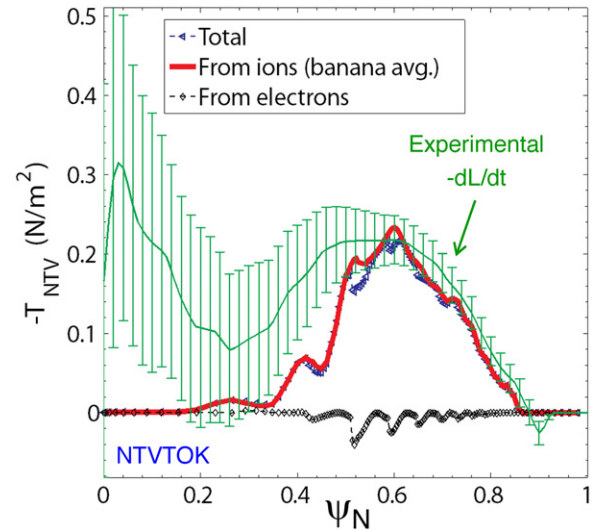
Rotation control is one component of a more comprehensive framework for stable operation. This capability is constituted in a disruption PAM framework under development for NSTX-U. The system consists of measurements of equilibrium, stability and divertor heat flux characteristics that serve as predictors. The measurements feed into control algorithms,

which are coupled to actuators that will steer the discharge towards stable operation. The measurements also feed into a disruption warning system, which uses a combination of individual sensor signals in an algorithm that yields an aggregate disruption warning level [5]. The algorithm can be tuned to detect impending disruptions with a 98% accuracy, which is a level required for ITER operation. If a clear disruption warning is issued, the system steers towards mitigation, rather than control.

The primary mitigation technique under development is the MGI system utilizing an improved electromagnetic valve similar to the design for the ITER system [52]. The MGI will use three such valves at different poloidal locations, one of them being the private flux region (PFR), to determine the location for maximum gas penetration. In parallel with experimental preparation, numerical efforts have been initiated with the DEGAS-2 Monte-Carlo code [53] to model the amount of gas the valves must inject to be consistent with the thermal and current quench time scales on ITER. Preliminary results indicate the penetration fraction of gas through the NSTX-U SOL to be in the range from 0.2 to 0.6 for D_2 and 0.8 to 0.9 for He across a range of SOL widths from 0.2 to 5 cm, electron temperatures from 1 to 100 eV, and electron densities from 10^{18} to 2×10^{20} m^{-3}. Greater penetration occurs for colder plasmas. For injection into the PFR, the penetration fractions increase to be in the range from 0.4 to 0.9 for D_2.

3. Develop solutions for the PMI

The second overarching research goal for NSTX-U is to develop solutions for the PMI. This topic covers both edge/divertor studies, including the characteristics and physics of the edge and sources of heat flux, as well as direct PMI studies that focus on material surface physics and chemistry.

3.1. Edge and divertor: structure and controlling processes

The application of pre-discharge lithium in NSTX has been shown to have beneficial effects for plasma confinement, pedestal structure and ELM suppression [54–57]. Recent analysis on this topic has focused on a dataset covering a wide, contiguous, range of pre-discharge lithium deposition amounts that can address discharge performance and pedestal evolution during and after ELM suppression [58]. The density pedestal shifted and widened continuously with increasing Li deposition even after ELMs were suppressed. No change was seen in the temperature pedestal location or width. At the pedestal top, it was primarily the electron temperature that changed continuously, along with the toroidal rotation and ion temperature. Efforts are underway to determine what controls the pedestal characteristics and why they continue to evolve even after ELMs are suppressed.

Previous studies addressing processes controlling these pedestal characteristics [56, 58] have expanded to studying the change in the microinstability properties of the plasma edge due to application of lithium through linear gyrokinetic calculations using the GS2 code [59]. For a discharge without the application of lithium, the calculations showed that microtearing modes were dominant at the top of the pedestal, which was located at $\Psi_n = 0.95$ (figure 19). With
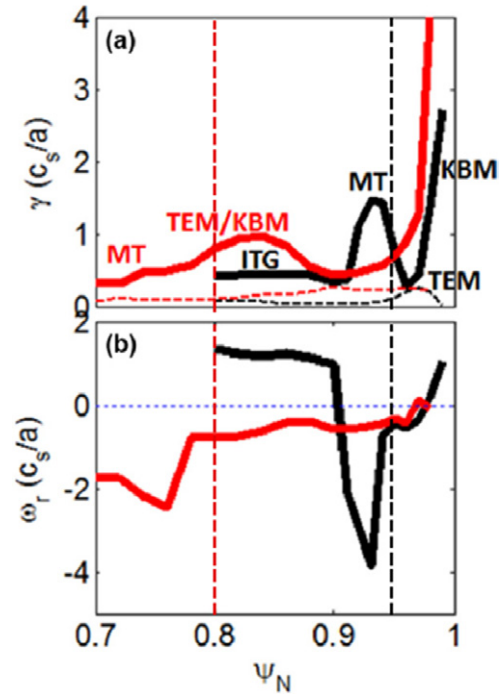

Figure 19. Linear growth rates (top) and real frequencies (bottom) of microturbulent modes in an unlithiated discharge (black) and a lithiated one (red). The black and red vertical lines indicate the location of the top of the density pedestal for the unlithiated and lithiated cases, respectively. (Reproduced from [59] courtesy of IAEA.)

lithium, the gradient region widened, the pedestal top moved in to $\Psi_n = 0.80$, and the density gradient at $\Psi_n = 0.95$ increased. The finite gradient at this location in the lithiated plasmas stabilizes the microtearing mode, and modes with characteristics like those of the trapped electron mode (TEM) and kinetic ballooning mode (KBM) became dominant, but with lower growth rates. Electron temperature gradient (ETG) modes were found to be unstable just inside the separatrix both with and without lithium, but with higher growth rates and a lower temperature threshold with Li, suggesting that ETG may play a role in limiting the electron temperature gradient in this region. At mid-pedestal, a hybrid TEM/KBM mode was found to be dominant with and without lithium. This hybrid mode was also identified in linear GENE [60] simulations during the last 20% of an ELM cycle near the pedestal top, similar to that found within the pedestal using GS2 [61].

Pulsed deuterium gas puffs were used to study possible modifications to the plasma edge profiles and edge turbulence and transport. A gas influx rate of 6.6×10^{21} deuterium atoms/s caused little or no change in the line-averaged plasma density or total stored energy, or in the edge density or electron temperature up to the time of the peak of the gas puff [62]. In addition, the radial profile of the D_α light emission and edge turbulence within this gas puff did not vary significantly over its rise and fall, implying that these puffs did not perturb significantly the local edge plasma or turbulence. DEGAS2 modelling of the puff indicated very low levels of radiation, consistent with the lack of change of T_e.

Numerical studies have been carried out to study the interaction of edge and SOL sheared flows with coherent
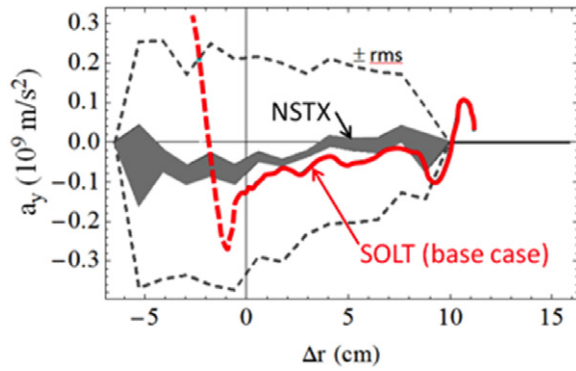
Figure 20. Poloidal Reynolds acceleration (a_y) for seeded blob simulations (red) compared with experimental results from gas puff imaging (grey). The black dashed lines represent experimental rms deviations. (Reproduced from [64] courtesy of IAEA.)

Figure 21. Change in divertor heat flux wetted area as a function of the number of ELM striations. (Reproduced from [69] courtesy of IAEA.)

turbulent structures, i.e. field-aligned blob filaments, which are a ubiquitous feature in the NSTX plasma edge, especially in the L-mode [63]. Results from seeded blob and quasi-steady-state turbulence simulations using the SOLT [64] code were compared with experimental data to evaluate the exchange of momentum between the blobs and flows. The simulations are based on a 2D curvature-interchange model, and they take into account physical mechanisms related to sheath currents and radial inhomogeneity for generation of Reynolds stress. The simulations reproduce many quantitative and qualitative features of the data, as measured by the gas puff imaging diagnostic, including size, scale-length and direction of approximately perpendicular flows, the inferred Reynolds acceleration (figure 20), the poloidal reversal of blob tracks and blob trapping and/or ejection. These results have implications for SOL interactions of blobs with PFCs. The radial penetration of blobs is influenced by flow shear, and thus judiciously driven sheared flows in the SOL could increase the SOL width if blobs influence this property.

3.2. Edge and divertor: heat flux and heat flux mitigation

An understanding of the processes controlling the heat flux profiles, and how they can be changed, is needed for projection of acceptable operating scenarios in future devices such as FNSF and ITER. Experiments on NSTX found that both high amounts of lithium wall conditioning and increasing plasma current can cause a strong contraction of the SOL heat flux width at the midplane [65]. The latter dependence is seen also at a high aspect ratio [66]. One potential method to modify the heat flux width is through controlled ELMs. Studies on JET and ASDEX-U indicated a broadening of λ_q with increasing ELM size, which could increase the size of tolerable ELMs in future devices [67, 68]. Results from NSTX, however, show that under certain circumstances the heat flux footprint during large ELMs could contract by up to 50%, exacerbating the heat flux challenge. Analysis of this data indicates that the heat flux profile broadening or narrowing is directly correlated with the number of filamentary striations measured in the ELM heat flux profile; profile narrowing is observed when very few or no striations are observed in the heat flux [69]. Figure 21 shows a measure of the change in the heat flux footprint wetted area by ELMs, relative to the value before the ELM, as a
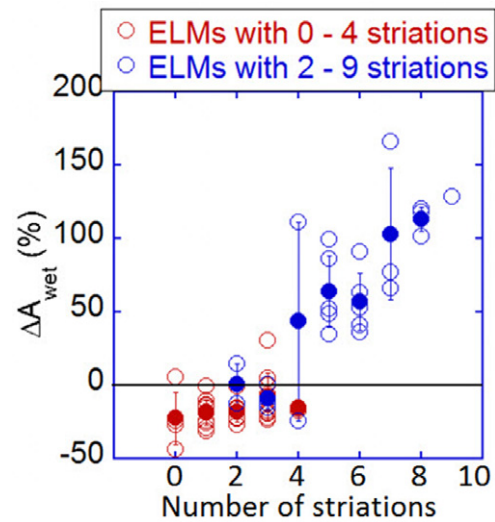
function of the number of ELM striations. The number of striations is inferred from 2D heat flux profiles that are from IR-based 2D surface temperature measurements coupled to a 3D heat conduction solver. The figure indicates the wetted area decreases and a peaking of the heat flux profile below ∼four striations. The wetted area increases almost linearly with the number of striations above this value.

The striations in the heat flux profile represent ELM filaments and, therefore, are believed to be related to the toroidal mode number of the ELMs before expulsion of the filaments. The typical range of toroidal mode numbers associated with ELM in NSTX is between one and five [57]. The implications of this result for ITER and FNSF need to be assessed by determining the edge stability and most likely toroidal mode number across a range of expected temperature and density profiles. In particular, scenarios that move the projected operating points up to higher n stability limits need to be identified in order to reduce the risk of peaking of the heat flux profiles during the ELMs.

The multi-fluid UEDGE [70, 71] has been used to assess snowflake [72] and impurity-seeded radiative divertors as heat flux mitigation candidates in NSTX-U. The simulations were carried out for NSTX-U plasmas with $I_p = 2\,\mathrm{MA}$, $B_T = 1\,\mathrm{T}$ and 9 MW of power flow into the SOL. NSTX H-mode-level transport coefficients were assumed; $\chi_{e,i}$ was taken to be $2\,\mathrm{m^2\,s^{-1}}$ at the core–edge interface ($\Psi_n = 0.9$), increasing to $4\,\mathrm{m^2\,s^{-1}}$ at the separatrix and remaining constant at that value in the SOL. The perpendicular particle transport increases from $D = 0.1\,\mathrm{m^2\,s^{-1}}$ at the core–edge interface, increasing to $0.5\,\mathrm{m^2\,s^{-1}}$ at the separatrix and SOL. The results of the simulation are shown in figure 22. Both standard and snowflake divertor configurations are found to be achievable using NSTX-U divertor coils, and the top panel shows the power to the divertor in both configurations (snowflake divertor in red, standard divertor in black) as a function of density at the core–edge interface, assuming 3% carbon in the plasma. The sudden change in power to the divertor at $\sim 4 \times 10^{19}\,\mathrm{m^{-3}}$ in the standard divertor configuration corresponds to where
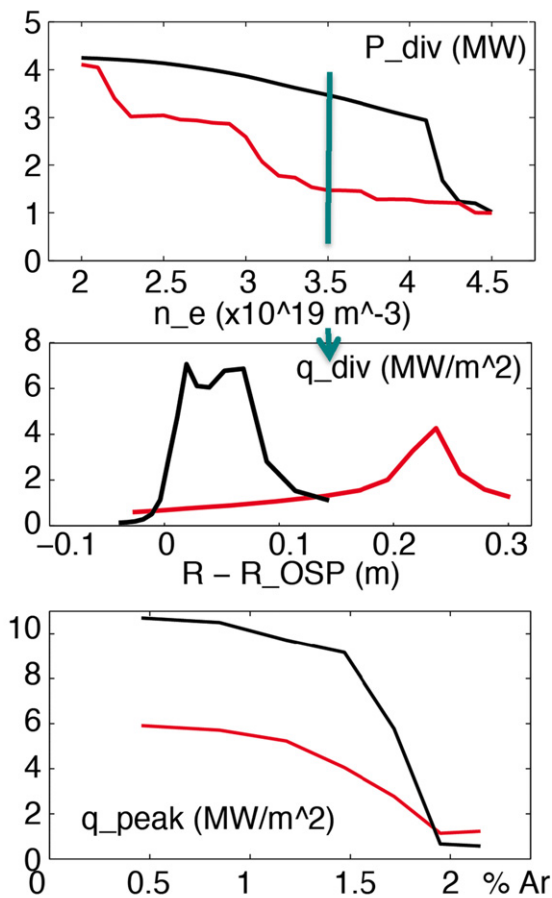
Figure 22. (Top panel) Total heat flux to the divertor in the snowflake (red) and standard (black) divertor configurations as a function of density at the core–edge interface ($\Psi_n = 0.9$). (Middle panel) Heat flux profiles at 3.5×10^{19} m^{-3} as a function of R_{OSP}, where R_{OSP} is the outer strike point radius. (Bottom panel) Heat flux to the divertor target as a function of % argon impurity seeding for 3.5×10^{19} m^{-3}.

the divertor detaches [73]. In the snowflake configuration, however, radiative, or detached operational densities extend down to $\sim 2 \times 10^{19}$ m^{-3}, corresponding to $n_e/n_{GW} \sim 0.4$. The total heat fluxes are reduced by ~ 70% at moderate densities ($\sim 3.5 \times 10^{19}$ m^{-3}), where the peak heat flux is reduced by 50% (middle panel). The bottom panel shows the peak heat flux as a function of % argon for the snowflake and standard divertors. It is clear that less impurity seeding is needed in the snowflake to attain lower heat fluxes.

3.3. Plasma–materials interaction

As lithium wall conditioning will be the preferred technique in NSTX-U, with eventual plans to test liquid lithium modules [74], studies have been conducted both in NSTX and in the laboratory to understand lithium–substrate interactions and the effect on both the deposited Li as well as on the substrates. Experiments in NSTX simultaneously addressed lithium sputtering from graphite tiles as well as from both heated and unheated liquid lithium divertor (LLD) modules, which had a molybdenum substrate [75]. Accumulation of carbon impurities was routinely observed in the core of ELM-free lithium-conditioned discharges in NSTX [76], but despite
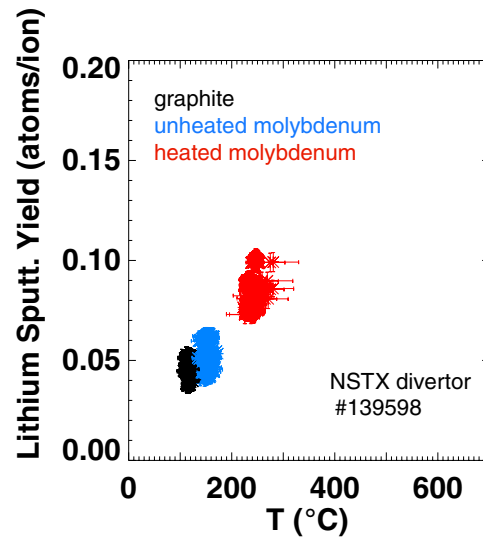

Figure 23. Lithium sputtering yield with unheated graphite and LLDs and heated LLDs.

even large Li deposition, Li concentrations in the plasma core were less than 1% of that of carbon [77]. This difference was partially explained by the difference in their core radial transport [76].

The temperature dependence of lithium sputtering due to impinging deuterium ions was studied both *in situ* and on a divertor test stand. The *in situ* measurements, shown in figure 23, were carried out only in a limited range of LLD temperatures, from 100 to 300 °C (the melting point of lithium is 180 °C). Li sputtering yields in atoms/incident D$^+$ for the graphite and unheated molybdenum surfaces (100–150 °C) were similar. With heating of the LLDs, and at temperatures above the Li melting temperature (250 to 300 °C), however, temperature-enhanced sputtering of the surface lithium was observed.

In order to expand the range of substrate temperatures being studied, and to mimic expected NSTX-U divertor conditions, test stand studies of lithium on these metal substrates were carried out on the MAGNUM-PSI linear device at DIFFER [78]. This supports the plan to install a row of TZM molybdenum tiles in the lower outboard divertor after the first run year of NSTX-U [79]. MAGNUM-PSI is a magnetized linear device designed for simulating divertor conditions expected in ITER-class devices, and it can also provide similar densities and temperatures as those found in NSTX. For NSTX-related experiments, a lithium evaporator was installed on MAGNUM-PSI, lithium was deposited onto a molybdenum substrate material, and then high-power D$^+$ discharges were created. Surface temperatures reached 1300 °C in these experiments. Results up to 700 °C will be shown. While high incident D$^+$ fluxes onto the target resulted in Li sputtering yields that increased with Li temperature up to 400 °C but then levelled off, the yields were lower than those predicted by low incident D$^+$ theory by two orders of magnitude due to lithium deuteride (LiD) formation (figure 24). Also observed in these experiments was the formation of an intense cloud of lithium emission directly in front of the target, which persisted for 3–4 s. This long-lasting intense vapour cloud resulted in a reduction of current to the
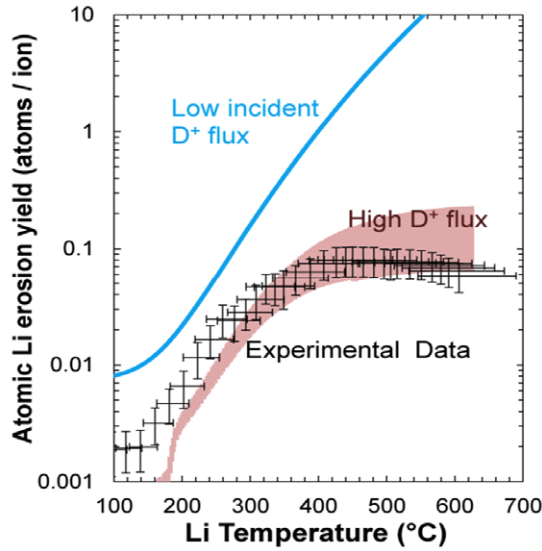
Figure 24. Lithium sputtering yields in the Magnum-PSI test stand as a function of lithium temperature for lithium-coated molybdenum substrates in a D^+ plasma. The blue curve and red region are modelling results.

target, and this offers the possibility for continuous divertor heat flux mitigation. Studies in NSTX-U will be performed to determine the maximum Li PFC temperature compatible with good confinement and reduced divertor heat flux.

Recent surface science experiments conducted at the Princeton Plasma Physics Laboratory have used x-ray photoelectron spectroscopy and temperature programmed desorption to understand the mechanisms for D retention in Li coatings on Mo substrates. The study shows that D is retained as LiD in metallic Li films. However, when oxygen is present in the film, either by diffusion from the subsurface at a high temperature or as a contaminant during the deposition process, Li oxides are formed that retain D as LiOD. Experiments indicate that LiD is more thermally stable than LiOD, which decomposes to liberate D_2 gas and D_2O at temperatures $100\,K$ lower than the LiD decomposition temperature. This result is consistent with the saturation of the Li emission yield with increasing temperature in the high D^+ flux scenario on MAGNUM-PSI. Furthermore, it highlights the importance of maintaining a metallic Li layer as the increased power loading expected in NSTX-U will reach elevated PFC temperatures during the course of a high-power discharge.

3.4. Integrated performance (core/pedestal/divertor)

Another means to modify the plasma edge and offer the potential for an operational regime of sustained high performance is the enhanced pedestal H- (EP H-) mode regime [56, 80]. EP H regimes were accessed in lithiated NSTX plasmas by a transition from an H-mode, often, but not always, triggered by an ELM. Confinement enhancements ($H_{98y,2}$) in the EP H-mode can be up to 50% over and above the already enhanced confinement in lithiated H-mode discharges. The EP H-mode is characterized by a region in the plasma edge with very sharp gradients in the ion temperature, typically a factor of three larger than those in the H-phase. There is also a localized region of large rotation shear in the vicinity of the
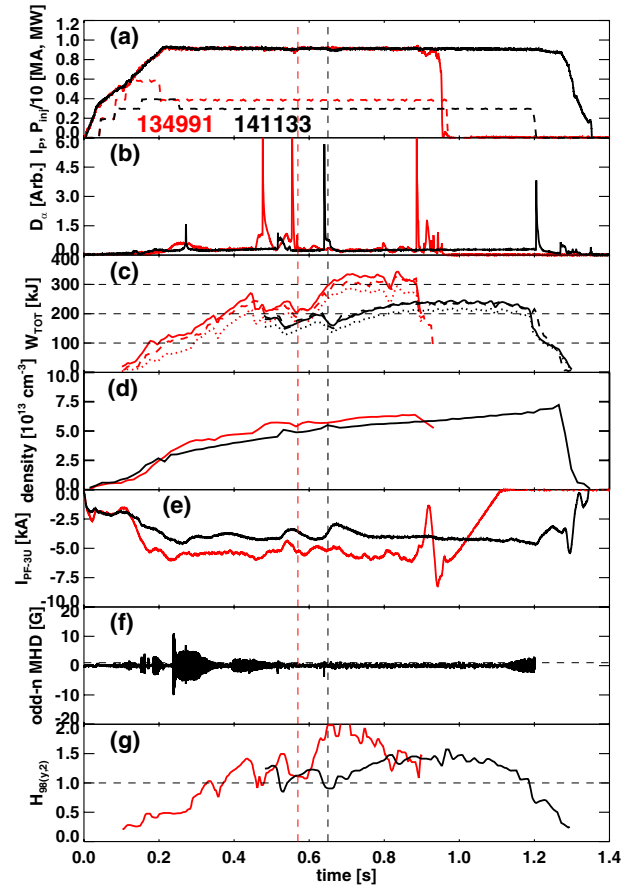

Figure 25. Time evolution of two long pulse EP H-modes. (Reproduced from [80] courtesy of IAEA.)

steep ion temperature gradient (ITG). No changes in low-*k* edge turbulence going from H to EP H, as measured by BES, were observed.

An example of the time evolution of two long-lived EP H-modes is shown in figure 25. Confinement enhancement factors ($H_{98y,2}$) of up to 1.7 were achieved in the shorter lived discharge, and up to 1.25 in the longer lived one, which also exhibited a period of near steady state for ~0.4 s. The quasi-stationary behaviour of the EP H-mode that was achieved suggests its potential for utilization as a high-performance regime on NSTX-U. However, it will be important to establish a reliable mechanism to trigger and control the transition to this regime. A strong velocity shear of the plasma edge is associated with the EPH-mode, and this may provide a clue as to the underlying physics causing the transition. Studies using triggered ELMs and specialized 3D edge MPs will be a focus of EP H-mode research on NSTX-U.

4. Explore unique ST parameter regimes to advance predictive capability for ITER and beyond

NSTX/NSTX-U operation at high ρ_i/a (low B_T), low ν_e^*, high beta ($\beta_n \geqslant 4$) and low aspect ratio provides a unique parameter regime giving high leverage for validating existing theory as well as for developing ST-specific frameworks. This will, in turn, lead to higher confidence predictions for devices at all aspect ratio, including ITER. This section will focus on
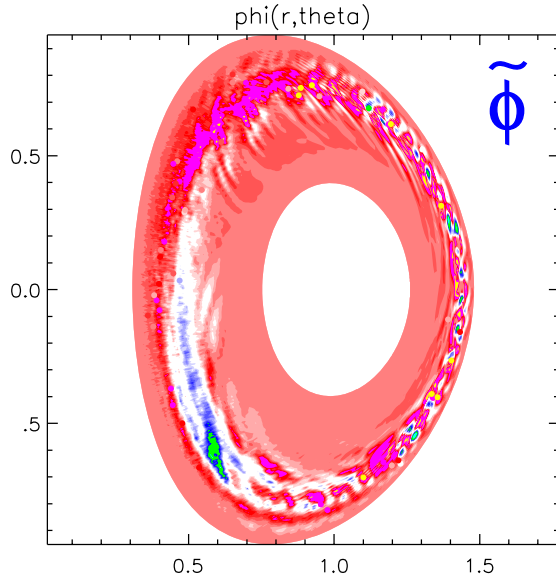
Figure 26. Non-linear GTS result showing electric potential perturbation for combined ITG/Kelvin–Helmholtz modes in an L-mode plasma. The abscissa major radius and the ordinate is vertical height (in m).

Figure 27. Comparison of experimental and GTS predicted thermal diffusivity for ions (left panel) and electrons (right panel). The experimental values of χ_e and χ_i were computed in TRANSP in interpretive mode, and the ion neoclassical value was computed using GTC-NEO. The abscissa is $x = [\Phi/\Phi_a]^{1/2}$, where Φ/Φ_a is the toroidal flux normalized to the value at the boundary.

aspects of transport and stability that have provided the basis for detailed comparisons to theory and theory development.

4.1. Thermal transport

The unique features of ST operation mentioned above results in a fusion plasma regime distinct from that of conventional aspect ratio tokamaks. In particular, because of the strong toroidal rotation, large ρ_i/a and strong toroidicity and shaping, it is crucial, while highly challenging, to use global gyrokinetic simulations to address turbulence and transport physics. Non-linear global gyrokinetic simulations of an NSTX L-mode plasma using the GTS [81] code have shown, for the first time, that a drift wave Kelvin–Helmholtz mode can be destabilized by strong toroidal rotation shear. This shear flow mode is characterized by finite $k_\parallel$ and broader k_θ than the ITG mode, which is also found to be present in the L-mode. Figure 26 shows the perturbed electric potential for the combined ITG and Kelvin–Helmholtz modes, which co-exist. The strong $E \times B$ shear can, at the same time, reduce the low-k fluctuations and associated transport linearly by changing the unstable mode family members and structure, and non-linearly by modifying the fluctuation amplitude and spectrum. However, even at the reduced level, the remaining low-k fluctuations, while contributing weakly to the observed highly anomalous electron thermal transport, can produce a significant ion thermal transport relevant to the experimental level in the outer core region. Figure 27 shows the comparison of the experimentally inferred ion (left) and electron (right) thermal diffusivities as computed in TRANSP, along with the turbulence-driven values predicted by GTS and the neoclassical value determined in GTC-NEO [82]. For the ions, the inferred and predicted profiles are within a factor of two in the outer core.

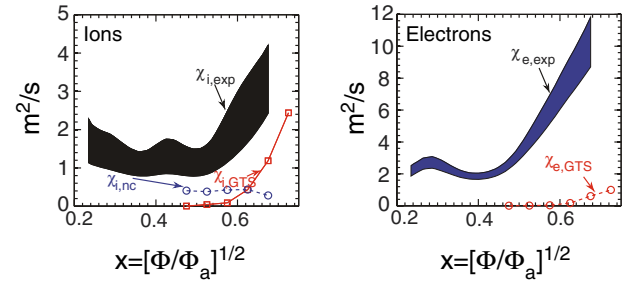Representative H-mode discharges were studied in detail as a basis for a time-evolving prediction of the electron temperature profile using an appropriate reduced transport model. For a high collisionality discharge, the time evolution of characteristic plasma variables such as β_e, ν_e^*, the MHD α parameter and the gradient scale lengths of T_e, T_i and n_e were examined as a prelude to performing linear gyrokinetic calculations using GYRO [83] to determine the fastest growing microinstability at various times and locations throughout the discharge. The inferences from the parameter evolutions and the linear stability calculations were consistent. Early in the discharge, when β_e and ν_e^* were relatively low, ballooning parity modes were dominant. As time progressed and both β_e and ν_e^* increased, microtearing became the dominant low-k_θ mode, especially in the outer half of the plasma. There are instances in time and radius where other modes, at higher k_θ, may be important for driving electron transport, in addition to the microtearing. Given these results, the Rebut–Lallia–Watkins (RLW) electron thermal diffusivity model, which is based on microtearing-induced transport [84, 85], was used to predict the time-evolving electron temperature across most of the profile. The results indicate that RLW does a good job of predicting T_e for times and locations where microtearing was determined to be important, but not as well when microtearing was predicted to be stable or subdominant [86].

Shown in figure 28 is a comparison of the linear growth rates (top panels) and predicted and measured T_e profiles (bottom panels) at representative times for two discharges at low and high collisionalities, respectively. In the top row, $\rho = r/a$, and the ρ values correspond to x values (bottom row) that are approximately 10% lower (e.g. $\rho = 0.7$ corresponds to $x = 0.6$). For the low $\nu_e^* \sim 0.06$ (left panels), the dominant microinstabilities have ballooning parity, and are identified as a hybrid TEM/KBM. For this discharge, the RLW model does a poor job of predicting the T_e profile. However, for the higher $\nu_e^* \sim 0.21$ discharge (right panel), where microtearing is calculated to be dominant, RLW does an excellent job in matching the T_e profile in the region from $x = 0.2$ to 0.8. Here, $x = \sqrt{\Phi/\Phi_a}$, where Φ/Φ_a is the local toroidal flux normalized to the boundary value. Inside of 0.2, an *ad hoc* χ_e was used as a proxy for transport induced by GAE/CAE modes in the very core, and $x = 0.8$ was chosen as the boundary. Identifying the reduced model that is able to predict electron temperatures in this unique ST parameter regime can lead to higher confidence extrapolations to future STs, such as FNSF and NSTX-U, where microtearing may be unstable.
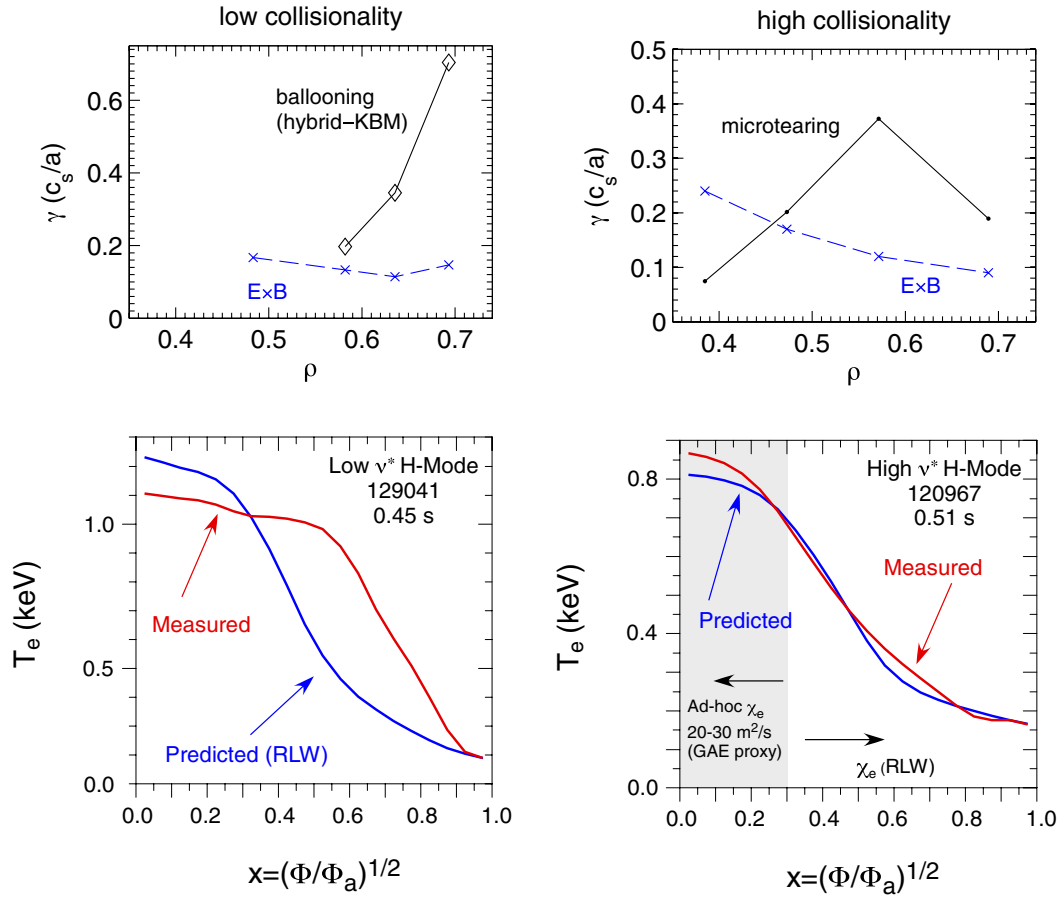
Figure 28. Linear growth rates (top) and measured versus predicted T_e using the RLW model (bottom) for a low (left) and high (right) collisionality H-mode discharge. In the top row, $\rho = r/a$, and the values correspond to x-values that are approximately 10% lower [86]. (Copyright 2014, American Institute of Physics.)

Highly non-linear electron thermal transport was observed in a set of RF-heated L-mode plasmas. It was observed that electron-scale turbulence spectral power, as measured by a high-k collective microwave scattering system at $r/a \sim 0.6$, was reduced significantly following the cessation of RF heating. The results clearly showed a time delay of about 1–2 ms between the RF cessation and the drop of about a factor of seven in measured electron-scale turbulence, indicating a causal relation between the two. In addition, the drop in turbulence spectral power happened on a 0.5–1 ms time scale, which is too fast for the standard local transport paradigm to provide a satisfying explanation. This is because that, while the drop in turbulence was on a fast time scale, there was virtually no change in the local equilibrium quantities that would be expected to drive the turbulence (e.g. a/L_{T_e}, a/L_{T_i}, a/L_{n_e}) on this time scale; the changes in these quantities occurred on confinement time scales (e.g. tens of milliseconds). The power balance analysis has shown about a factor of two decrease in the electron thermal transport after the sudden drop in turbulence. Linear stability analysis has shown that both ion- and electron-scale microinstabilities are unstable in the high-k measurement region, and that, linearly, the profiles are well above marginal stability. Two explanations are being explored for this non-linear response through non-linear global gyrokinetic simulations. The first is one of high

profile stiffness, so that even nearly negligible changes in driving gradients can lead to large changes in turbulence and transport. The second is on of flux-driven transport, which would inherently be a non-local phenomenon. A decrease in local heat flux, due to changes in some other region of the plasma, leads to a decrease in the turbulence responsible for the transport. Recent non-linear gyrokinetic simulations support the non-local transport hypothesis.

First detailed measurements of changes of high-k turbulence across the L–H transition have also been made with the microwave scattering system. While low-frequency activity was seen to be relatively benign after the L–H transition, the D_α signal exhibited dithering for approximately 12 ms after the transition. It was after this period of dithering that the edge transport barrier at $r/a > 0.9$, typical of the H-mode, was established. The high-k scattering system measured turbulence at $r/a = 0.7$ to 0.8, and it showed a factor of seven suppression of the turbulence amplitude after the transition, for $k_\perp < 9$ to 10, down to ~ 2. The dithering of the D_α after the L–H transition was associated with dithering of the high-k turbulence, but with no set phase relation between the two. BES measurements of low-k turbulence at the same location exhibited similar temporal intermittency as in the high-k measurement. Linear stability calculations indicated a drop in ETG growth rates after the L–H transition, consistent with the
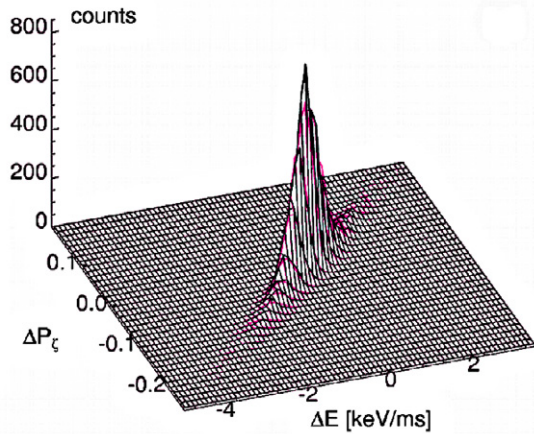
Figure 29. Calculated fast ion transport probability distribution function for TAE avalanches.

drop in the measured high-k turbulence amplitude, although the observed intermittence requires a non-linear process.

4.2. Momentum and impurity transport

Linear gyrokinetic analysis has been used to study the source of anomalous momentum and impurity transport in NSTX. In NSTX H-mode plasmas, perturbation experiments indicated the existence of a significant inward momentum pinch [47, 87]. Gyrokinetic calculations for L-mode plasmas indicate that the inward momentum pinch is small and weakly dependent on many parameters, except for aspect ratio, where the pinch becomes much larger (inward) as R/a increases to over two. In H-mode plasmas, where either microtearing or KBMs dominate, simulations indicated only a small outward pinch, which is insensitive to parameter variations.

For impurity transport, the linear gyrokinetic calculations indicate an inward carbon pinch when KBMs dominate, which is inconsistent with experimental observations [88]. Consequently, local linear theory does not appear to explain either the momentum or impurity transport in NSTX. Work is underway to investigate non-linear and non-local effects. Preliminary global, non-linear GTS calculations indicate that the low-k fluctuations in L-modes, which was discussed earlier, can produce significant toroidal momentum flux, including a large anti-gradient residual stress due mainly to zonal flow shear induced $k_\parallel$ spectrum asymmetry.

4.3. Fast ion transport

There has also been much progress in developing the predictive capability to model the effects of some of the AE scenarios discussed in section 2.2 on the fast ion distribution. This development of reduced fast ion transport models is critical to being able to develop precise discharge scenarios that allow for achieving optimal heating and current drive. There are two methods that are presently under development.

The first method uses a probability distribution function that produces changes in a particle's phase space coordinates (energy and canonical toroidal momentum) through 'kicks' due to a resonant interaction with a given set of instabilities [89]. In this reduced model, the transport
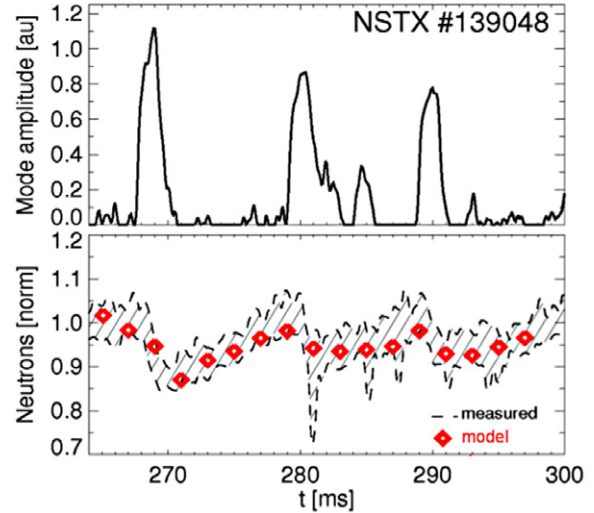

Figure 30. Calculated (red) and measured (black) neutron rate versus time (bottom panel). The calculated neutron rate is derived from the kick model using the mode amplitudes shown in the top panel.

probability function, $p(\Delta E, \Delta P_\zeta/P_\zeta, E, \mu)$ is computed from analytic theory as well as particle-following codes such as ORBIT or SPIRAL (figure 29). The size of the phase space kicks are taken to scale linearly with mode amplitude, which can be computed from an observable quantity such as the neutron rate and the ideal mode structure as computed by NOVA [90]. This model can thus provide the detailed evolution of F_{NB} (E, P_ζ, μ) and hence accurate estimates for NB-driven current. The model has been implemented in the standalone NUBEAM code, and initial benchmarks indicate good agreement between the normalized calculated and measured neutron rates in an NSTX discharge with bursting TAE activity (figure 30). This model is presently being implemented in the full TRANSP code.

In parallel, a 1.5D quasi-linear (QL), critical gradient model (CGM) is being developed. This model is based on computing the critical fast ion profile gradient in the presence of unstable AEs [91]. The model uses analytic growth and damping rates for TAEs to compute a critical fast ion beta profile under the assumption that the quasi-linear diffusion from overlapping resonances is applicable. The applicability of the CGM requires a large number of such modes with no or minor bursting/chirping at saturation. Similar conditions can be envisioned for ITER-like burning plasmas in a variety of plasma scenarios. In practice, the fast ion profile is computed in TRANSP, and if the calculated profile is larger than the computed critical value, the profile is relaxed through the 1.5D-QL model to the critical value. Comparing the relaxed profile to the initial one enables evaluation of fast ion losses and other quantities. The CGM was validated against DIII-D data, and good agreement was reported [92]. Initial benchmarking with NSTX data, comparing the experimental neutron reduction $(1 - \frac{S_{\text{measured}}}{S_{\text{classical}}})$, where $S_{\text{classical}}$ is computed in TRANSP, to that predicted by the CGM for the observed modes, also shows good agreement (figure 31).
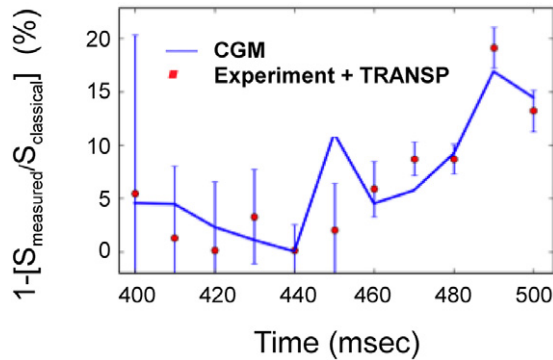
Figure 31. Experimental neutron reduction and that predicted by the critical gradient model for an NSTX plasma.

4.4. Stability

Modes driven unstable above the pressure-driven, no wall kink limit can constrain fusion performance. One much studied mode, the RWM, has relatively slow growth rates ($\gamma \tau_{\text{wall}} \sim 1$), and, as previously discussed, can be stabilized by kinetic effects and passive and active feedback control. In plasmas with stable RWM, an ideal wall mode (IWM) can be driven unstable near the ideal wall limit. The IWM has much higher frequencies and growth rates than the RWM. Recent MARS-K linear calculations have shown that, similar to the RWM, both rotation and kinetic effects can modify IWM stability limits. At low-β ($\beta_n < 3.5$), the kinetic effects are minimal, with the kinetic stability limit similar to the fluid limit, and both are consistent with the experimental β_n for $n = 1$ mode onset when the experimental rotation is used. For $\beta_n \sim 5$, the kinetic limit is consistent with the experimental limit, while the fluid limit leads to an underprediction of the β for mode onset. A similar conclusion holds for the highest β ($\beta_n \sim 6$ to 6.5).

5. Conclusions

NSTX results in the three overarching areas discussed in this paper have set the stage for achieving the research goals of the NSTX-Upgrade device. These goals, once again, include producing stable, 100% non-inductive operation in high-performance plasmas, assessing plasma–material interface solutions to handle the high heat loads expected in the next-step devices and exploring the unique ST parameter regimes to advance predictive capability. NSTX-Upgrade, with twice the plasma current and toroidal field of NSTX, with pulse lengths up to 5 s, and with a second more tangentially aimed neutral beam, will provide the capability for addressing these goals and thus for developing the physics basis for an ST-based Fusion Nuclear Science Facility. Physics research operations in NSTX-U will commence in mid-2015.

Acknowledgments

References

[1] Menard J.E. *et al* 2012 *Nucl. Fusion* **52** 083015
[2] Abdou M.A. *et al* 1996 *Fusion Technol.* **29** 1
[3] Menard J.E. *et al* 2011 *Nucl. Fusion* **51** 103014
[4] Gerhardt S.P. *et al* 2012 *Nucl. Fusion* **52** 083020
[5] Gerhardt S.P. *et al* 2013 *Nucl. Fusion* **53** 043020
[6] Sabbagh S.A. *et al* 2013 *Nucl. Fusion* **53** 104007
[7] Berkery J.W. *et al* 2014 *Phys. Plasmas* **21** 056112
[8] Morris A.W. *et al* 2014 *IEEE Trans. Plasma Sci.* **42** 402
[9] Raman R. *et al* 2011 *Phys. Plasmas* **18** 092504
[10] Redd A.J. *et al* 2009 *J. Fusion Energy* **28** 203
[11] Jardin S.C., Pomphrey N. and Delucia J. 1986 *J. Comput. Phys.* **66** 481
[12] Raman R. *et al* 2013 *Nucl. Fusion* **53** 073017
[13] Sovenic C.R. *et al* 2004 *J. Comput. Phys.* **195** 355
[14] Hooper E.B. *et al* 2013 *Phys. Plasmas* **20** 092510
[15] Ebrahimi F. *et al* 2013 *Phys. Plasmas* **20** 090702
[16] Taylor G. *et al* 2010 *Phys. Plasmas* **17** 056114
[17] Jaeger E.F. *et al* 2001 *Phys. Plasmas* **8** 1573
[18] Bertelli N. *et al* 2014 *Nucl. Fusion* **54** 083004
[19] Perkins R.J. *et al* 2013 *Nucl. Fusion* **53** 083025
[20] Kallman J. *et al* 2010 *Rev. Sci. Instrum.* **81** 10E117
[21] Perkins R.J. *et al* 2014 The contribution of RF rectification to field-aligned losses of HHFW power to the divertor in NSTX *Nucl. Fusion* submitted
[22] Fredrickson E.D. *et al* 2013 *Nucl. Fusion* **53** 013006
[23] Fredrickson E.D. *et al* 2013 *Phys. Plasmas* **20** 042112
[24] Wang F. *et al* 2013 *Phys. Plasmas* **20** 072506
[25] Park W. *et al* 1999 *Phys. Plasmas* **6** 1796
[26] Wang F. *et al* 2013 *Phys. Plasmas* **20** 102506
[27] Belova E.V., Gorelenkov N.N. and Cheng C.Z. 2003 *Phys. Plasmas* **10** 3240
[28] Fredrickson E.D. *et al* 2001 *Phys. Rev. Lett.* **87** 145001
[29] Crocker N.A. *et al* 2013 *Nucl. Fusion* **53** 043017
[30] Stutman D. *et al* 2009 *Phys. Rev. Lett.* **102** 115002
[31] Bortolon A. *et al* 2013 *Phys. Rev. Lett.* **110** 265008
[32] Kramer G.J. *et al* 2013 *Plasma Phys. Control. Fusion* **55** 025053
[33] Ferraro N.M. and Jardin S.C. 2009 *J. Comput. Phys.* **228** 7742
[34] Hawryluk R.J. 1980 An empirical approach to tokamak transport *Physics of Plasmas Close to Thermonuclear Conditions: Proc. Course (Varenna, Italy, 1979)* vol 1, p 19
[35] Hirshman S.P. and Whitson J.C. 1983 *Phys. Fluids* **26** 3553
[36] Spong D.A. *et al* 2001 *Nucl. Fusion* **41** 711
[37] Kritz A.H. *et al* 1982 Ray tracing study of electron-cyclotron heating in toroidal geometry *Proc. 3rd Joint Varenna–Grenoble Int. Symp. on Heating in Toroidal Plasmas(Grenoble, France, 1982)* vol 2, p 707 www.iaea.org/inis/collection/NCLCollectionStore/_Public/14/770/14770102.pdf
[38] Lin-Liu Y.R., Chan V.S. and Prater R. 2003 *Phys. Plasmas* **10** 4064
[39] Brambilla M. 1999 *Plasma Phys. Control. Fusion* **41** 1
[40] Kaye S.M. *et al* 1988 *Nucl. Fusion* **28** 1963
[41] Bondeson A. and Ward D. 1994 *Phys. Rev. Lett.* **72** 2709
[42] Hu B. and Betti R. 2004 *Phys. Rev. Lett.* **93** 105002
[43] Berkery J.W. *et al* 2014 *Phys. Plasmas* **21** 052505
[44] Berkery J.W. *et al* 2010 *Phys. Plasmas* **17** 082504
[45] Shaing K.C. and Callen J.D. 1983 *Phys. Fluids* **26** 3315
[46] Pankin A. *et al* 2004 *Comput. Phys. Commun.* **159** 157
[47] Solomon W. *et al* 2009 *Phys. Rev. Lett.* **101** 065004
[48] Zhu W. *et al* 2006 *Phys. Rev. Lett.* **96** 225002
[49] Kim K. *et al* 2014 *Nucl. Fusion* **54** 073014
[50] Park J.-K., Boozer A.H. and Glasser A.H. 2011 *Phys. Plasmas* **14** 052110
[51] Sun Y. *et al* 2011 *Nucl. Fusion* **51** 053015
[52] Raman R. *et al* 2014 *Rev. Sci. Instrum.* **85** 11E801
[53] Stotler D.P. and Karney C.F.F. 1994 *Contrib. Plasma Phys.* **34** 392
[54] Mansfield D. *et al* 2009 *J. Nucl. Mater.* **390–391** 764
[55] Maingi R. *et al* 2009 *Phys. Rev. Lett.* **103** 075001
[56] Maingi R. *et al* 2010 *Phys. Rev. Lett.* **105** 135004
[57] Boyle D.P. *et al* 2011 *Plasma Phys. Control. Fusion* **53** 105011

[58] Boyle D.P. *et al* 2013 *J. Nucl. Mater.* **438** S979
[59] Canik J.M. *et al* 2013 *Nucl. Fusion* **53** 113016
[60] Jenko F. *et al* 2000 *Phys. Plasmas* **7** 1904
[61] Diallo A. *et al* 2013 *Nucl. Fusion* **53** 093026
[62] Zweben S.W. *et al* 2014 *Plasma Phys. Control. Fusion* **56** 095010
[63] Zweben S.W. *et al* 2004 *Nucl. Fusion* **44** 134
[64] Myra J.R., Davis W.M. and D'Ippolito D.A. 2013 *Nucl. Fusion* **53** 073013
[65] Gray T.K. *et al* 2014 *Nucl. Fusion* **54** 043013
[66] Eich T. *et al* 2013 *J. Nucl. Mater.* **438** S72
[67] Eich T. *et al* 2011 *J. Nucl. Mater.* **415** S856
[68] Devaux S. *et al* 2011 *J. Nucl. Mater.* **415** S865
[69] Ahn J.-W. *et al* 2014 *Nucl. Fusion* **54** 122004
[70] Rognlien T.D. *et al* 1992 *J. Nucl. Mater.* **196** 347
[71] Rognlien T.D. and Rensink M.E. 2002 *Fusion Eng. Des.* **60** 497
[72] Ryutov D.D. 2007 *Phys. Plasmas* **14** 064502
[73] Meier E.T. *et al* 2014 Modeling divertor concepts for spherical tokamaks NSTX-U and ST-FNSF *Nucl. Fusion* submitted
[74] Jaworski M.A. *et al* 2013 *Plasma Phys. Control. Fusion* **55** 124040
[75] Kugel H.W. *et al* 2010 *Fusion Eng. Des.* **85** 865
[76] Scotti F. *et al* 2014 *J. Nucl. Mater.* **439** 1
[77] Podesta M.A. *et al* 2012 *Nucl. Fusion* **52** 037001
[78] DeTEMMERMAN C.G. *et al* 2012 *J. Vac. Sci. Technol.* A **30** 041306
[79] Kaita R. *et al* 2014 Addressing the challenges of plasma–surface interactions in NSTX-U *IEEE Trans. Plasma Sci.* submitted
[80] Gerhardt S.P. *et al* 2014 *Nucl. Fusion* **54** 083021
[81] Wang W. *et al* 2010 *Phys. Plasmas* **17** 072511
[82] Wang W. *et al* 2004 *Comput. Phys. Commun.* **164** 178
[83] Candy J. and Waltz R. 2003 *J. Comput. Phys.* **186** 545
[84] Rebut P.H. and Brusati M. 1986 *Plasma Phys. Control. Fusion* **28** 113
[85] Rebut P.H., Lallia P.P. and Watkins M.L. 1988 The critical temperature gradient model of plasma transport: applications for JET and future tokamaks *Proc. 12th IAEA Conf. on Plasma Physics and Controlled Nuclear Fusion Research (Nice, France, 1988)* Paper D-4-1 www.iaea.org/inis/collection/NCLCollectionStore/_Public/21/008/21008733.pdf#page=209
[86] Kaye S.M. *et al* 2014 *Phys. Plasmas* **21** 082510
[87] Kaye S.M. *et al* 2009 *Nucl. Fusion* **49** 045010
[88] Scotti F. *et al* 2013 *Nucl. Fusion* **53** 083001
[89] Podesta M., Gorelenkova M. and White R. 2014 *Plasma Phys. Control. Fusion* **56** 055003
[90] Cheng C.Z. and Chance M. 1987 *J. Comput. Phys.* **71** 124
[91] Ghantous K. *et al* 2012 *Phys. Plasmas* **19** 092511
[92] Heidbrink W.W. *et al* 2013 *Nucl. Fusion* **53** 093006